Coseismic Underground Rupture, Geometry, Historical Surface Deformations and Seismic Potentials of the March 28, 2019 Mw 5.04 Mangya earthquake fault

Shengli Wang, Wujun Wu, Qinghong Li, Chao Li, Yongxiang Li, Yan Chen, Liangshu Wang, Mingjie Xu, Zhi Guo

Coseismic Underground Rupture, Geometry, Historical Surface Deformations and Seismic Potentials of the March 28, 2019 *Mw* 5.04 Mangya earthquake fault

Shengli Wang[1]*, Wujun Wu[1, 2]*, Qinghong Li[3], Chao Li[1]†, Yongxiang Li[1], Yan Chen[4], Liangshu Wang[1], Mingjie Xu[1], Zhi Guo[5]

[1]School of Earth Sciences and Engineering, Nanjing University, Nanjing, China

[2]Key Laboratory of Reservoir Characterization, Research Institute of Petroleum Exploration and Development-Northwest, PetroChina, Lanzhou, China

[3]CNPC Xibu Drilling Engineering Company Limited, Urumqi, China

[4]Univ. Orléans, CNRS, BRGM, ISTO, UMR 7327, F-45071, Orléans, France

[5]Institute of Geology, China Earthquake Administration, Beijing, China

Corresponding author: ShengLi Wang (wangsl@nju.edu.cn)

*Shengli Wang and Wujun Wu contributed equally to the study and are co-first authors.

†Current address: School of Earth Sciences and Engineering, Hohai University, Nanjing, China

Abstract

The March 28, 2019 *Mw* 5.04 Mangya earthquake damaged eight ongoing drilling boreholes in the oil-production Yingxiong Ling (YXL) area, southwestern Qaidam of northern Tibet. The borehole damages provide an opportunity to measure directly the coseismic slips, the rupture area, and the seismic moment. The damages reveal the underground rupture area of 45.30 ± 10.24 km^2, the maximum slip of 400 ± 13 mm, and the seismogenic fault dip of ~38.6°. These parameters generate a seismic moment of (1.81 ± 0.47) $\times 10^{17}$ Nm and a moment magnitude of 5.47 ± 0.16. Seismic exploration reveals that the geometry of the SZG ramp, the uppermost part of the multi-bend Yingxiong Ling thrust system, agrees primarily with the rupture plane derived from the borehole damages and one plane of the focal mechanism solution. This suggests that this earthquake resulted from slipping on the ramp. The hanging wall of the YXL thrust system forms the complex fault-bend fold YXL anticlinorium. Active thrusting and folding along both edges of YXL attest to the southwestern vergence of this thrust system. Growth strata demonstrate average slip rates of the thrust system ranging from ~0.2 mm/yr to ~0.3 mm/yr. The thrusted and folded recent alluviums along the southwestern edge indicate two thrusting events with coseismic slips of 1.7 ± 0.15 m and 3.5 ± 0.15 m at 6.16 ± 0.52 ka and ~35.91 ka, respectively. The entire rupturing of the thrust system can produce *Mw* 7.65 ± 0.03 earthquakes.

Keywords: the March 28, 2019 *Mw* 5.04 Mangya earthquake; coseismic rupture; seismic potential; Yingxiong Ling; Qaidam; Tibet

1 Introduction

Earthquakes occur due to sudden shear slip on faults within the Earth. Although some geophysical, geodetic (e.g., Feng et al., 2010; Xu et al., 2010) and morphotectonic techniques (e.g. Xu et al., 2009; Liu-Zeng et al., 2009) are available to estimate coseismic slips and rupture areas, precisely quantifying coseismic slips without surface ruptures occurring in a several-second time scale remains a grand challenge, particularly for addressing issues, such as fault propagation, fault interaction, and assessing the moment magnitude. Under certain favorable circumstances, coseismic slips may be recorded by offsets of features that penetrate a fault plane, including geomorphic markers and/or artificial structures. However, these circumstances are scarce.

Here, we describe a case example that the coseismic rupture of the March 28, 2019 Mangya earthquake fault in southwestern Qaidam, northern Tibet (Figure 1) can be retrieved by quantifying damages of eight ongoing drilling boreholes and drilling tools. With the records of this event, we determine the coseismic slip and rupture area of the earthquake fault. Also, we present three seismic profiles to analyze the geometry, seismic potentials, and the long-term slip rates of the earthquake fault.

2 Geological Setting

The Himalayan-Tibetan orogen went through subduction mountain building, terrane accretion untill present continent-continent collisional mountain building (e.g., Yin and Harrison, 2000). Persistent Indian indentation into Eurasia resulted in the growth of the Tibetan plateau (e.g., Tapponnier et al., 2001; Zuza et al., 2019), large-scale shortening in central Asia (Molar and Tapponnier, 1975; Tapponnier and Molar, 1979; Chen et al., 1993) and extrusion of East and Southeast Asia (Tapponnier and Molnar, 1976; 1977; Tapponnier et al., 1982). The western Kunlun range, the Altyn Tagh fault and the Qilian range initiated to form the northern edge of the Tibetan plateau shortly after the Indo-Tibetan collision (e.g., Yin et al., 2002; 2008a; Pang et al., 2019; Zuza et al., 2019; Chen et al., 2002), and persist presently (e.g., Wang et al., 2017a). The Qaidam Basin, the largest active hinterland one with an average elevation of ~3000 m in northern Tibet, is bounded by the Altyn Tagh fault in the northwest, the Qilian Shan in the northeast, and the Eastern Kunlun in the south (Figure 1b), and elevated by sediments infilling (e.g., Tapponnier et al., 2001; Wang et al., 2014). NW–NWW trending folds are widespread all over Qaidam (e.g., Qinghai BGMR, 1991; Zhou et al., 2006; Yin et al., 2007; 2008a; 2008b; Chen et al., 2010; Wu et al., 2013; Pan et al., 2015; Cheng et al., 2018).

Yingxiong Ling (YXL) is an active NW-trending anticlinorium with its highest peak of ~3835 m in southwestern Qaidam (Figure 1a), consisting of the Shizigou-Yousha Shan (SZG-YSS) anticline in the southwest, the Ganchaigou (GCG) anticline in the middle, and the Xianshuiquan-Youquanzi (XSQ-YQZ) anticline in the northeast (Figure 1a; Yin et al., 2007; Yu et al., 2011; Pan et al., 2015; Cheng et al., 2018; Huang et al., 2018; Bian et al., 2019; Wu et al., 2020).

Cenozoic stratigraphic divisions and age assignments of southwestern Qaidam are based on terrestrial fossils (e.g., spores, ostracods, and pollen) found in outcrop sections, magnetostratigraphy, fission-track, detrital $^{40}Ar/^{39}Ar$ dating, and the basin-wide stratigraphic correlation of outcrop geology and drill cores with seismic profiles (Huo, 1990; Qinghai B.G.M.R., 1991; Yang et al., 1992; Song and Wang, 1993; Huang et al., 1996; Xia et al., 2001; Qiu, 2002; Sun et al., 2005; Rieser et al., 2006a, 2006b; Chang et al., 2015; Wang et al., 2017; Cheng et al., 2019). Major Cenozoic stratigraphic units include the Lulehe ($E_{1-2}l$), the lower (E_3^1xg) and upper (E_3^2xg) members of the Xiaganchaigou, the Shangganchaigou (N_1sg), the Xiayousha Shan (N_2^1sy), the Shangyousha Shan (N_2^2sy), the Shizigou (N_2^3s), and the Qigequan (Q_1q) Formations. We refer to Bian et al.'s (2019) summary for the Cenozoic stratigraphy of the YXL region (Table 1).

Before the March 28, 2019 Mw 5.04 Mangya earthquake occurred in YXL, southwestern Qaidam of northtern Tibet (Figure 1b; USGS, 2019; China Earthquake Data Center, 2019), the January 2, 1977 *Mw* 6.4 and *Mw* 5.1, and the February 26, 1987 *M* 6.1 earthquakes were recorded in this region (Wang et al., 1999). Since the Qaidam Basin is the largest hydrocarbon-bearing hinterland sedimentary basin in the Tibetan Plateau (Horton et al., 2012), high-quality and high-resolution exploration seismic data have been achieved to explore the deep structural trap in this area (e.g., Yin et al., 2007; 208a; 208b; Chen et al., 2010; Wu et al., 2013; Pan et al., 2015; Bian et al., 2019; Wu et al., 2020). Active folding and thrusting deformed recent alluviums and abandoned geographic markers along the southwestern edges of YXL (Xu et al., 2018a; 2018b). Moreover, as the epicenter of this event at YXL is located in the mature oil-production region, exploration and development of hydrocarbon offer numerous high-quality seismic data and well logs with on-going drilling boreholes, and provide a solid base for addressing these issues.

3 The coseismic underground slips of the March 28, 2019 Mangya earthquake fault

Dense boreholes have been drilled in the zone of YXL where locates the epicenter of the March 28, 2019 Mw 5.04 Mangya earthquake (Figures 1b and 2); eight ongoing drilled boreholes were directly damaged by the coseismic underground slip of the earthquake fault. They are namely H4-3-414, H4-3-510, H4, H6-2-510, H4-2-506, H2-3-413, H4-3-411, and H4-2-510 (Figure 2). The damage types include bit freezing and cutting of drilling rods and casing pipes.

3.1 Slip at borehole H4-3-414

Drilling of borehole H4-3-414 was finished on March 25, 2019. When the instruments of transmission logging were intruding to the depth of ~2590 m at 5:36, the earthquake happened. The drilling rods were stuck on the mainshock and could not be moved. An aftershock occurred at 7:20. After releasing stuck and pulling out, the drilling rod was broken off (Figures 3a and b) and the logging tools fell into the hole. The kink-like bend and breaking-off of the drilling pipe (Figures 3a and b) indicate that it was sheared to break off completely by a low-angle thrust. A 165-mm-diameter lead seal was put into the hole and was stuck at the depth of ~2034.79 m, and then was pulled out. Its side face has scratches (Figure 4c), demonstrating that the lead seal passed by the upper fracture of the 196.8-mm-diameter casing pipe when the lead seal was put into and/or pulled out from the hole through the cutoff of the casing pipe. And the bottom of the lead seal is clear (Figure 4d), indicating that it did not touch the lower fracture of the casing pipe, and the casing pipe was sheared to break off completely at the depth of ~2034.79 m. Therefore, the offset of the casing pipe is more than its outer diameter of 196.85 mm. Assuming that the kink-like deformation of the drilling rod is symmetrical with respect to the broken surface and the rod is just broken away (Figures 3c–g), the offset is 400 ± 13 mm (Figure 3g) in the scenario of the sum of the kink-like width of 250 ± 13 mm (Figure 3g), and the difference of 149.87 mm (Figure 3f) between the inner diameter (166.63 mm) of the casing pipe and the double drilling rod wall thickness (16.76 mm). The error results from the rugged fracture surface of the broken drilling pipe.

3.2 Slip at borehole H4-3-510

Borehole H4-3-510 was being drilled to the depth of ~4323 m when the earthquake happened. The suspending weight of the drilling rods and tools was ~850 KN before the earthquake, increased suddenly to ~1700 KN on the shock, and then decreased to ~400 KN after the shock. The pressure of the pump for drilling fluid circulation decreased to null and the loss of circulation occurred after the shock, indicating that the drilling fluid leaked to break off the return of the circulation, and that the casing pipe was severely broken. After the shock, the suspending weight of the uplifting drilling rods and tools of ~400 kN demonstrates that parts of the drilling rods and tools were disjointed. Two make-ups did not work, and so the drilling rods and tools were not connected. The drilling rods and tools pulled out from the hole is ~2110.47 m long, so the fish of the drilling rods and tools assemblage kept in the borehole is ~2212.53 m in length. The cutting surface of the uplifted drilling rod reveals that the intermediate casing strings were sheared off by the coseismic slip of the earthquake fault at the depth of ~2110.47 m to result in leaving the fish in the borehole. Therefore, we deduce that the offset of the drilling rod is more than the diameter of the intermediate casing strings of 196.85 mm. The damage of borehole H4-3-510 is identical to that of borehole H4-3-414 in the scenario of Figures 3f and g.

3.3 Slip at borehole H4

When borehole H4 was being drilled to the depth of ~4417.17 m, the earthquake happened. On pulling up the drilling rods and tools, its suspending weight increased from ~940 KN to ~1000 KN, implying that a part of the drilling rods was stuck, but not broken off. About 9 m^3 of drilling fluid with a density of 1.98 g/cm^3 leaked, revealing that a casing pipe was squeezed to break and to stick a drilling rod. The depth of the drilling rod sticking is ~1700 m, determined from pulling drilling rods up. The drilling rod sticking indicates that the offset of the casing pipe is no more than 149.87 mm, the difference between the inner diameter (166.63 mm) of the casing pipe and the double-wall thickness (16.76 mm) of a drilling rod, as the drilling rod is completely squashed (Figure 3f), and is no less than the difference of 65.03 mm between the inner diameter of the casing pipe and the outer diameter (101.60 mm) of the drilling rod, as both sides of the drilling rod just touches the casing pipe (Figure 3e). Therefore, the coseismic displacement at this borehole is 107 ± 42 mm.

3.4 Slip at borehole H6-2-510

When a loss of circulation of borehole H6-2-510 was being handled, the earthquake occurred. After the main shock, naked drilling rods were put into the borehole and got tight at the depth of ~1994.74 m, implying that the casing pipe was severely deformed at that depth. Its offset is more than the difference of 108.21 mm between the inner diameter (247.91 mm) of the intermediate casing string and the outer diameter (139.70 mm) of the drill rod sub, similar to the scenario of Figue 3e, which is the minimum amount of deformation. However, the deformed borehole was made a wiper trip by processing milling taper and casing milling, indicating that the diameter of the deformed intermediate casing string at the depth is more than the minimum diameter (124 mm) and less than the maximum (240 mm) of the milling taper. Thus, the coseismic displacement at this site is 182 ± 58 mm. The borehole logging (Table 2) shows deformations from the depth of 1970 m to 1990 m. The amount of deformation is significantly less than what we deduced at the depth of ~1994.74 m.

3.5 Slip at borehole H4-2-506

When a loss of drilling fluid circulation of borehole H4-2-506 was being handled, the earthquake occurred. After the main shock, naked drilling rods were put into the borehole to the depth of 3674 m and then were pulled up to the depth of 1000 m on March 28, indicating that the coseismic deformation of the borehole is significantly less than the difference of 79.61 mm between the diameter (168.3 mm) of the drilling pipe sub and the inner diameter (247.91 mm) of the intermediate casing string. However, a 241.3-mm-diameter drill bit was put into the borehole and got tight at the depth of ~1925 mm on March 31, demonstrating that the casing pipe was squeezed. Its offset should be more than the difference of 6.61 mm between the inner diameter (247.91 mm) of the intermediate casing string and the diameter (241.30 mm) of the drill bit, which is the minimum amount of deformation. The borehole logging (Table 2) shows that the maximum is 48.40 mm. Therefore, the total offset of the borehole is more than 6.61 mm and less 48.40 mm at the depth of ~1925 m, this is to say that the slip at this borehole site is 28 ± 21 mm.

3.6 Slip at borehole H2-3-413

The coseismic slip of the Mangya earthquake fault deformed the casing pipe of borehole H2-3-413 to stick the drilling rod at the depth of ~1500.0 m when the drilling rods were being pulled up after the borehole inclination had been measured. The borehole had been drilled to the depth of ~1899 m. The coseismic drilling pipe sticking indicates that the slip at this site is no less than the difference of 128.27 mm between the inner diameter (255.27 mm) of the casing pipe and the outer diameter (127 mm) of the drilling rod, as both sides of the drilling rod just touched the casing pipe (similar to the situation of Figure 3e), and no more than 236.89 mm, the difference between the inner diameter of the casing pipe and the double-wall thickness (18.38 mm) of the drilling rod, as the drilling pipe was completely squashed (similar to the situation of Figure 3f). Therefore, the coseismic displacement at this site is 188 ± 59 mm.

3.7 Slip at borehole H4-3-411

The Mangya earthquake happened when borehole H4-3-411 was being drilled to the depth of ~2159 m. The coseismic slip of the earthquake fault deformed the casing pipe to stick the drilling rod. However, the sticking depth was weakly constrained. The sticking was not released by many methods, indicating that the deformation of casing pipes and drilling rods of borehole H4-3-411 are identical to those of borehole H2-3-413. So, the coseismic slip at the borehole site is 188 ± 59 mm.

3.8 Slip at borehole H4-2-510

The mainshock occurred when boreholes H4-2-510 was being drilled to the depth of 4828 m. Just after the main shock, it was found that drilling pipes got stuck, indicating the coseismic deformation of the borehole. The stuck depth was measured at ~2271 m by pulling up drilling rods. The sticking of the drilling rods indicates that the casing pipe at the stuck depth was squeezed to extrude the drilling rod at that depth. As the drilling rod was completely pressed to flat (the situation of Figure 3f), the offset of the borehole at the stuck depth is 149.87 mm, the difference between the inner diameter (166.63 mm) of the casing pipe and the double-wall thickness (16.76 mm) of the drilling rod. As both sides of the drilling rod just touched the casing pipe (the situation of Figure 3e), the offset is the difference of 65.03 mm between the inner diameter of the casing pipe and the outer diameter (101.60 mm) of the drilling pipe. So, the coseismic displacement at this borehole site is 107 ± 42 mm.

3.9 Coseismic underground rupture area

Boreholes H4-3-510 and H4-3-411 have the maximum offsets. The amount of offsets decreases northwestwards and southwestwards from these two boreholes. In the northeast and southeast of them, coseismic slips are not well constrained due to the lack of ongoing drilling wells. Nonetheless, we may assume that the coseismic slips decrease radially and linearly with distances away from the point of the maximum slip. The coseismic slips at the eight boreholes indicate that the maximum slip of 400 ± 13 mm locates proximately at the center between boreholes H4-3-510 and H4-3-414. Using linear interpolation and extrapolation, we fit a contour map of coseismic slips (Figure 2). The fitted contour map presents an ellipse shape with a half long axis of 4.01 ± 0.45 km and a half short axis of 2.81 ± 0.32 km.

An ellipse area is defined as

$$ARA = \pi\ a\ b \tag{1}$$

where a is the half length of the long axis, b is the half length of the short axis, and ARA is the area of the projected ellipse. The projected area of the coseismic rupture of 35.40 ± 8.00 km^2 is therefore obtained.

These eight damaged boreholes reveal their coseismic slips on the earthquake fault plane and rupture depths (Table 3). Boreholes H4-3-414, H4-3-510, H4, H6-2-510, and H4-2-506 were drilled by PertoChina; their construction records and earthquake damages are detailed, precise, and reliable. However, boreholes H2-3-413, H4-3-411, and H4-2-510 were outsourced; their construction records and earthquake damages are rather simple, less precise and undependable; but their locations and damages are reliable. Thus, we use the parameters of the first five boreholes to fit a plane. The plane formulae is

$$z = -0.336x -0.726y + 13274438.528 \tag{2}$$

with a dip angle of 38.6°. This dip is slightly contrast to the attitude of plane 1 determined from the focal mechanism solution of the Mangya earthquake (Table 4).

Therefore, the true rupture area is given as

$$RA = ARA/\cos\alpha \tag{3}$$

where RA is the true rupture area, ARA is the area of projected ellipse, and α is the dip angle of the fault plane. Using the fitted dip angel, the projected area, and formula (3), the true underground coseismic rupture area of 45.30 ± 10.24 km^2 can be generated. This value may be a lower limit of the Mangya earthquake fault rupture since the eight boreholes are primarily located in the western part of the deductive rupture area.

3.10 The measured seismic moment and the moment magnitude

Damages of the boreholes reveal the true coseismic rupture area and slips. The moment magnitude can be thus determined by the relations

$$M_0 = \mu\ A\ S \tag{4}$$

where M_0 is the seismic moment, μ is the shear modulus, A is the faulted area, and S is the average slip over the faulted area, and

$$Mw = 2/3 \log M_0 - 6.03 \tag{5}$$

where Mw is the moment magnitude. Adopting the measured faulted area for A, the coseismic slips for S decreasing radially and linearly away from the maximum point, and the shear modulus of 30 $\times 10^9$ N/m^2, M_0 of (1.81 ± 0.47) $\times 10^{17}$ Nm and Mw of 5.47 ± 0.16 can be produced.

4 Geometries of the YXL anticlinorium and the YXL thrust system

We present three seismic profiles in Figures 5, 6 and 7 to decipher the geometries of the March 28, 2019 Mangya earthquake fault and the YXL anticlinorium. These seismic profiles image a sub-horizontal reflector, crossing other inclined reflectors (Figures 5, 6 and 7) at their uppermost parts. Drilling and well logging reveal that this sub-horizontal reflector presents the groundwater level. Figure 5 shows the geometry of the entire middle YXL anticlinorium. Figure 6 approximately crosses perpendicularly the northwestern SZG-YSS anticline near the coseismic rupture region of the Mangya earthquake fault (Figures 1 and 2). Figure 7 crosses the southeastern SZG-YSS anticline. Formation boundaries in these seismic profiles are defined based on fossils from drilling cores, lithology and synthetic seismogram, and therefore correlate to seismic reflectors. According to characteristics of the seismic reflector assemblage, formation boundaries are extrapolated to neighboring profiles. We invoke the fault-related folding theories (Suppe, 1983; Suppe and Medwedeef, 1990; Medwedeef and Suppe, 1997), growth strata theory (Suppe et al., 1992) and the kink method to interpret these seismic profiles in finer scales to decipher the geometries of the YXL anticlinorium and the YXL thrust system.

4.1 The YXL anticlinorium

We interpret YXL as a complex fault-bend fold anticlinorium, produced by the southwest-vergent thrusting of the YXL thrust system (Figures 5a and b). The northwestern SZG-YSS anticline is made up of a breakthrough fault-propagation fold anticline on surface and a wedge structure in depth (Figures 5b and 6b), and the southeastern SZG-YSS anticline (Figure 7a and b) is a forelimb breakthrough fault-propagation fold anticline (see Appendix A for a complete description).

The kink-band width of 3.5 ± 0.2 km between the axial surfaces A and A' (Figure 6b) reveals the slip along the lower SZG ramp in the northwestern SZG-YSS anticline. The bottom age of the growth strata in the northeast limb of the northwestern SZG-YSS anticline is interpolated at 17.2 ± 1.0 Ma based on the thickness (Figure 6b), with the ages of ~15.3 Ma and ~22.0 Ma for the top and bottom of the Xiayousha Shan Formation, respectively (Bian et al., 2019). These parameters produce an average slip rate of ~0.2 mm/yr for the lower SZG ramp.

The kink width between the axial surfaces A'' and A in the southeastern SZG-YSS anticline stands for a slip of ~4.67 km along the YSS ramp (Figure 7b). Using the ages of the top and bottom of the Xiayousha Shan Formation, the basal age of the growth strata is interpolated at 16.5 ± 1.0 Ma which is slightly younger than that of the northwestern segment of the anticline. These parameters produce an average slip rate of 0.3 mm/yr for the SZG ramp, which is slightly higher than that of the lower SZG ramp.

We interpret the GCG ridge as a classic fault-bend fold anticline based on locating regions of homogeneous dip (see Appendix B for a complete description; Figures 5a and b), and XSQ-YQZ as a multi-bend fault-bend fold anticline (see Appendix C for a complete description; Figures 5a and b).

4.2 The YXL thrust system

Detailed structural interpretation and analysis indicate that the YXL anticlinorium is generated by the southwest-vergent thrusting of the multi-bend faults, namely the YXL thrust system (Figure 5b). The YXL thrust system in the northwestern YXL anticlinorium consists of the SZG ramp, the SZG back-ramp, the SZG flat, the lower SZG ramp, the GCG ramp, the XSQ flat, the upper XSQ ramp, the lower XSQ ramp, and the lower XSQ flat (Figures 5b and 6b). The thrust fault system, generating the SZG-YSS anticline, changes as the YSS ramp and the YSS flat (Figure 7b) in the southeastern YXL anticlinorium, with the SZG back-ramp waning.

The northwestern SZG-YSS comprises two stacked anticlines (Figures 5b and 6b). The outcropping one is a forelimb breakthrough fault-propagation fold anticline with the high-angle or overturned forelimb (Figures 8 and 9) and the sub-horizontal crest (Figure 8); and the buried lower SZG wedge structure is a fault-bend fold anticline (Figures 5b and 6b), which is considered as the main hydrocarbon production trap in the YXL region. According to the fault-bend folding theory (Suppe, 1983), the width of ~3.48 km of the back-limb (the kind-band between the axial surfaces A and A') of the lower SZG anticline (Figure 6b) is equal to the slip along the lower SZG ramp. Figure 6b shows that the hanging wall ramp width is ~3.70 km, approximately matching the prediction of the classic fault-bend folding theory (Suppe, 1983).

The length of ~4.96 km of the forelimb along the fault and the back limb kink width of 5.42 km of the GCG anticline (Figure 6b) correspond to the slips before and after folding, respectively, approximately complying with the fault-bend folding theory (Suppe, 1983). However, the slip transferred forward from the GCG flat is significantly larger than the back limb kink width of northwestern SZG-YSS. The excess slip should be accommodated by the growth of the surface fault-propagation fold and movement along the break-through thrust ramp (Figures 5b and 6b).

The slip along the XSQ flat, the upper and the lower XSQ ramps can be obtained by the displacement of ~4.56 km of the bottom of the Lulehe Formation, which is slightly less than the slip of ~5.42 km along the GCG flat. This discrepancy probably results from the estimate of the length of the lower XSQ ramp and the bias in the time-depth conversion of the seismic profile.

4.3 The Shaxi wedge structure

The seismic profiles image well the Shaxi wedge structure (Figures 5 and 6), southwest of YXL. We interpret Shaxi as a wedge structure resulting from a northeat-vergent displacement of the thrust sheet to fold the strata above it to form a monocline based on locating regions of homogeneous dip and axial surfaces (see Appendix D for a complete description; Figures 5b and 6b). The growth axial surface Gs and the active axial surface M terminate in the middle part of the Shangyousha Shan Formation (Figures 5b and 6b), indicating its inactivity after deposition of this layer. This interpretation demonstrates that the width of ~3.57 km of the kind band between M and M' (Figures 5b and 6b) represents the slip of the thrust. We interpolate the top and bottom ages of the growth strata at ~10.4 Ma and ~36.8 Ma, respectively, according to the top and bottom depths of the growth strata in Figure 6 and the formation boundary ages (Bian et al., 2019). These parameters produce an average slip rate of ~0.13 mm/yr of the blind thrust. The seismic profiles (Figures 5b and 6b) show that the Shaxi structure and the YXL structures have no kinematic links.

5 Surface deformations resulting from activity of the YXL thrust system

The borehole deformations and historical earthquakes (Wang et al., 1999) reveal that the multi-bend YXL thrust system is active. The hanging wall of the thrust system penetrates through active axial surfaces to fold inevitably recent alluviums and abandoned geomorphic markers (Suppe, 1983; Suppe et al., 1992; 1997). We observed that recent alluviums and geomorphic markers are folded and cut along both edges of YXL during our reconnaissance in the summer of 2019.

5.1 Active thrusting and folding along the southwestern edge of YXL

Fine-scale analysis of seismic profiles reveals that the traces of the SZG ramp and the active axial surface B' constitute the southwestern edge of northwestern YXL (Figures 5b and 6b). The SZG ramp trace marks the southwestern surface border of northwestern YXL; the mountainous northwestern SZG-YSS anticline locates in its northeast; and there exists the desert covered by recent alluviums (Figure 8) in its southwest. The active axial surface B' denotes the underground southwestern border of northwestern YXL (Figures 5b and 6b).

5.1.1 Active thrusting

The SZG ramp breaks through the southwestern limb of northwestern SZG-YSS and thrusts to the ground surface (Figures 1, 5b, 6b, 8, and 9; Xu et al., 2018a; 2018b). The modified river-cut section (Figures 9a and b) shows that the SZG ramp displaces the Qigequan Formation and recent alluviums. Unit A is folded and truncated by F3 (Figure 9b). The southwestern part of the fold in Unit A is partially eroded; and Unit B laps on the erosional surface (Figure 9b). Folding of Unit A implies a thrusting event. The middle and lower parts of Unit B1 are truncated by F3; its upper part is folded to form an anticline. F3 refracts to a lower angel at a higher level and vanishes in the middle part of Unit B1. The top of folded Unit B1 is eroded. Folding and truncation of Unit B1 indicate another thrusting event. Unit C deposits on both sides of the folded Unit B1. Unit C1 covers the folded Unit B1 and Unit C (Figure 9b). These features indicate that there is no more thrusting event rupturing the ground surface after the deposition of Units C and C1.

The basal age of Unit A is 39.77 ± 6.38 ka. The middle Unit B1 has an age of 32.63 ± 2.27 ka. The boundary age between Unit B1 and Unit C is 6.16 ± 0.52 ka (Xu et al. 2018a). Therefore, the thrusting event recorded by folding of Unit A is in the age bracket between 39.77 ± 6.38 ka to and 32.63 ± 2.27 ka. The event represented by folding of Unit B1 slightly postdates 6.16 ± 0.52 ka. The displacement of Unit B and Unit B1 indicates that the coseismic slip of the last event is 1.70 ± 0.15 m at this site (Figure 9b). The error is resulted from identifying the boundary of sedimentary units, which is no more than 0.15 m.

5.1.2 Active folding

The active axial surface B' fixes to the tip of the SZG wedge structure and extends to the ground surface (Figures 5b and 8) or terminates below the SZG ramp (Figure 6b). With the southwest-vergent thrusting by the wedge structure, the active axial surface B' passes through and folds recent alluviums, and abandoned geomorphic markers. Along the most southwestern edge of YXL, the axial surface B' is located to the southwest of the SZG ramp (Figure 8). Therefore, the fold scarp corresponding to the axial surface B' is located to the southwest of the SZG ramp trace (Figures 8, 10a and 10b). The topographic profile crossing the southwestern edge of SZG-YSS has two inflection points (Figures 10a and 10b). One is at the outcrop of the SZG ramp, and another is at the trace of the axial surface B' (Figures 10a and 10b). The sub-horizontal topography in the northeast of the SZG indicates that the hanging wall uplifts as a rigid block; and the topographic slope between the ramp and the axial surface B' is ~9.9% (or ~5.7°), which is significantly steeper than ~2.9% (or ~1.7°) of the desert surface in the southwest of YXL (Figure 10b).

A trench exposes recent alluviums (Figures 11a and 11b). Among them, Upg1 through Upg4 maintain the constant thickness and the dip angle. Ug1 laps on Upg4 and pinches out at ~8.2 m (Figure 11b). Ug2 laps on Ug1 to tapers out at ~4.7 m (Figure 11b). Ug3 is an aeolian sediment layer with the constant thickness, covering Upg4, Ug1, and Ug2 in disconformity. Ug4, a constant thickness layer of alluviums, rests on Ug3. Upg1 through Ug2 have an identical angle, indicating that they widen by kink band migration. The width of the kink bands increases gradually with the thrusting of the SZG wedge structure (Figure 11c). Pinch-outs of Ug1 and Ug2 represent two thrusting events of the wedge structure in depth. Their total widths are not exposed, but their difference is 3.5 ± 0.15 m, providing the coseismic displacement of the buried wedge structure during the thrusting event represented by the pinch-out of Ug1. The age of the lower-middle Ug1 is 94.93 ± 7.98 ka, and the age of the middle Ug3 is 59.43 ± 3.42 ka. They bracket the age of this thrusting event, but closer to 94.93 ± 7.98 ka. The definite sedimentary record of the event is the boundary between Ug1 and Ug2. The sedimentation rate of Ug3 and Ug4 accelerates to cover folded Ug2. Folding of these sediments (Figure 11b) indicates that the trench does not cross the axial surface B', which may be approximately located at the dashed rectangular in Figure 11c. The top envelope dip angle of the growth strata (Figure 11c) is in response to the topographic slope between the SZG ramp trace and the axial surface B' (Figures 10a and 10b), which is smaller than the angle of the kink band over the lower SZG wedge structure (Figures 11a, 11b and 11c).

5.2 Active folding along the northeastern edge of YXL

The northeastern edge of YXL is an active fold scarp (Figures 12 and 13). In the northeast of the scarp, there exists an even playa covered by alluviums and diluviums. In the southwest of the scarp, there are rugged and inaccessible mountains of YXL. The northwesternmost part of YXL along the scarp is eroded to form a planation surface being ca. 30 m higher than the playa, marking the border of the low-angle northeastern limb of the XSQ-YQZ anticline (Figures 12, 13a and c). The seasonal stream-cut section (Figure 13a) shows that gravel layer T on the southwestern scarp tread descends northeastwards and splits from the topographic surface. Recent alluviums are folded and thin out toward the scarp (Figures 13a and c). Dips of the alluviums below the T level become higher southwestwards to equal to the dip of the Qigequan Formation. At the scarp, the Qigequan Formation is covered by recent alluviums to form a growth unconformity (Figures 13a and c). Long topographic profiles crossing the scarp show the scarp height of ~30–31 m (Figures 13b and d).

6. Discussion

We present the coseismic slips, rupture area, seismic moment, moment magnitude, geometry, and historical deformation of the March 28, 2019 Mangya Mw 5.04 earthquake fault. These new findings can improve our understanding of mechanisms of earthquakes and active tectonics in the northwestern Qaidam Basin, northern Tibet.

6.1 The relationship between the coseismic underground slip, the SZG ramp and the March 28, 2019 Mangya earthquake

The measured underground rupture area and the slips along the SZG ramp suggest an earthquake of *Mw* 5.47 ± 0.16. This result is comparable with *Mw* 5.04, *Ms* 5.0 (China Earthquake Data Center, 2019) and Mw 4.8 ± 0.117 (USGS, 2019) obtained from seismic wave inversion.

The mainshock and aftershocks measured by China Earthquake Data Center (2019) and USGS (2019) are not exactly in the extent derived from borehole deformations (Figure 2). However, the shock occurrence times are the same; therefore, they should record the same shocks. Moreover, the focus depths of the main shock of 10 ± 1.8 km (USGS, 2019), 9 ± 1.8 km (China Earthquake Data Center, 2019) and ~9.5 km have been reported, which are significantly distinct from the depths of the coseismic rupture ranging from ~1700 m – ~2110 m. Nevertheless, the depths of the coseismic rupture are identical with the SZG ramp (Figures 6a and 6b). The time of the borehole deformation is the same as the mainshock. The magnitude predicted by the true coseismic underground rupture area and slips approximates the measured magnitudes. One plane of the focal mechanism solution of the mainshock is identical to the results derived from borehole deformation and hydrocarbon seismic exploration. The SZG ramp is the only active fault evidenced by surface geology observations. Therefore, we conclude that the SZG ramp, the uppermost segment of the YXL thrust system, is the seismogenic fault of the March 28, 2019 *Mw* 5.04 Mangya earthquake, considering large uncertainties in measurements of the focus depths and epicenters.

6.2 Seismic potentials of the YXL thrust system

Seismic exploration reveals the geometry of the SZG ramp, the uppermost segment of the YXL thrust system. The surface deformation along both edges of YXL demonstrates that the entire YXL thrust system is active. Accordingly, we suggest that the earthquakes of the January 2, 1977 *M* 6.4 and *M* 5.1, as well as the February 26, 1987 *M* 6.1 at the YXL area (Wang et al., 1999) were generated by thrusting of one part of the YXL thrust system. These thrusting events in recent decades did not rupture or fold ground surface and recent alluviums. This phenomenon suggests that the small-scale coseismic slips of these thrusting events are locked by an unruptured segment in front of the ruptured segments to accumulate more elastic strain in the hanging wall.

Alternatively, these slips may be completely absorbed by the growth of the YXL anticlinorium.

The surface ruptures and folded alluviums indicate that the coseismic slip per event can reach up to 1.7 ± 0.15 m – 3.5 ± 0.15 m, suggesting that the entire YXL thrust system probably ruptures. Seismic exploration shows that the YXL thrust system underlies the YXL anticlinorium. We can approximately use the surface extent of 3200 ± 160 km^2 of the anticlinorium as the area of the thrust system, ignoring the changes in its geometry. Using the equations (3) and (4), with the fault area of 3200 ± 160 km^2, the average coseismic slips of 1.7 ± 0.15 m and 3.5 ± 0.15 m over the thrust system as well as the shear modulus of 30×10^9 N/m^2, *Mw* 7.44 ± 0.18 and *Mw* 7.65 ± 0.03 can be obtained. This estimate means that the entire rupture of the YXL thrust system has the potential to generate *Mw* 7.65 ± 0.03 earthquakes. If each segment ruptures separately, the thrust system can produce earthquakes with magnitudes less than *Mw* ~7.6.

6.3 Growth mechanism the YXL anticlinorium

Surface deformation and seismic interpretation indicate that the southwest-directed thrusting to fold the hanging wall of the YXL thrust system to form the anticlinorium. The growth of the YXL anticlinorium creates the highest peak of ~3835m at the core of the GCG anticline, decreasing southeastwards to the average elevation of ~3000 m of the Qaidam Basin. This suggests that the displacements of the YXL thrust system wane southeastwards. Growth strata indicate that the SZG-YSS anticline has been initiated since the early Middle Miocene (~16.5 – ~17.2 Ma).

7 Conclusions

The SZG ramp, the uppermost part of the YXL thrust system, is the seismogenic fault of the March 28, 2019 Mw 5.04 Mangya earthquake. The partial SZG ramp ruptured during this event with a rupture area of 45.30 ± 10.24 km^2, a maximum slip of 400 ± 13 mm and the fault dip of ~38.6°. These parameters generate a seismic moment of (1.81 ± 0.47) $\times 10^{17}$ Nm and a moment magnitude of 5.47 ± 0.16. The long-term average slips of the thrust system range from ~0.2 mm/yr to 0.3 mm/yr since the early Middle Miocene. The ramp of the thrust system ruptured the ground surface along the southwestern edge of YXL at ~35.91 ka and 6.16 ± 0.52 ka. The last thrusting event has a coseismic slip of 1.7 ± 0.15 m. The earlier coseismic folding events indicate that the coseismic displacement of the thrust system can reach up to 3.5 ± 0.15 m. The YXL thrust system has the potential to generate *Mw* 7.65 ± 0.03 earthquakes. Growth strata indicate that YXL has been initiated since the early Middle Miocene (~16.5 – ~17.2 Ma).

Appendix A: The SZG-YSS anticline and its related fault

The ~60-km-long SZG-YSS anticline trends northwest and plunges toward the southeast at the Mangya Lake. The anticline is divided into the NW, middle and SE segments based on changes in trends of its axial trace (Figure 1). The axis of the NW segment strikes northwest. The SW limb of the NW segment dipping northeast is overturned at high angles (Figure 8), and is cut by the SZG ramp. The core of the NW segment is composed of the broad, sub-horizontal Shangyousha Shan Formation (Figure 8). The NE limb of the NW segment consists of the Shangyousha Shan and the Shizigou

Formations dipping toward the northwest at ~25°. The middle segment strikes north-south. The sub-vertical or somewhere overturned SW limb of this segment is made up of the Shangganchaigou Formation. The sub-horizontal Shangganchaigou Formation crops out in the core of this segment. The NE limb contains the Shangyousha Shan and Shizigou Formations dipping toward the northeast-east at ~15°. The axis of the SE segment strikes northwest. The SW limb of this segment contains the sub-vertical or slightly overturned Xiayousha Shan, Shangyousha Shan, and Shizigou Formations. Its core consists of the horizontal Xiayousha Shan Formation. The NE limb of this segment includes the Xiayousha Shan, Shangyousha Shan and Shizigou Formations dipping to the northeast at ~10°.

The profiles of Figures 5a, 5b, 6a and 6b cross southwestwards the Shizigou segment of the SZG-YSS anticline. We analyzed the fine changes in attitudes of seismic reflectors to locate a few regions of homogenous dip. There exist continuous reflectors covering the SZG-YSS anticline. At the crest of the anticline, there exist sub-horizontal reflectors between the axial surfaces C and C' from the ground surface to the SZG ramp. Below the growth axial surface G, the reflectors between the active axial surface A and the inactive axial surface A' dip to the northeast at ~13º. Northeast of the axial surface C and above the growth axial surface G, there are sub-horizontal reflectors. Below the SZG ramp, northeast of the axial surface B' and above the SZG back ramp, there exist curved reflectors with dips ranging from ~15º to ~26º. Above the SZG flat, below the SZG back-ramp and southwest of the axial surface B, there exist reflectors dipping to the southwest at ~23º; there are horizontal reflectors between the axial surfaces B and A', and below the SZG back-ramp; there exist reflectors dipping to the northeast at ~13° between the axial surfaces A and A', and below the growth axial surface G. These three regions of homogeneous dip constitute the lower SZG wedge structure, a buried fault-bend fold anticline (Figures 5b and 6b). There are the horizontal regions of homogeneous dip between the axial surfaces A and D' and above the GCG flat, constituting the syncline between the SZG-YSS and the GCG anticlines. Below the SZG flat, the lower SZG ramp, and the GCG flat are regional low-angle reflectors (Figures 5b and 6b).

We put forward the structural interpretation of the southwestern SZG-YSS anticline (Figures 5b and 6b) based on above-mentioned locating of regions of homogeneous dip. The well-imaged fault reflectors define the northeast-dipping SZG ramp, separating the arcuate reflectors below it from the noisy region representing the high angled overturned SW limb of the NW SZG-YSS anticline above it (Figures 5a, 5b, 6a and 6b). Reflectors above and below the SZG back-ramp are disharmonious, which evidences the fault; the SZG back-ramp terminates upward at the lower end of the axial surface C' to connect with the SZG ramp. The axial surface B' terminates downward at the SZG wedge tip and upward below the SZG back-ramp. The SZG flat occurs between lower ends of the axial surface B and B'. The connection of the downward terminations of the axial surfaces A and A' is interpreted as the lower SZG ramp. The connection of the downward terminations of axial surfaces A and D' is interpreted as the GCG flat. This structural interpretation (Figures 5b and 6b) predicts that the southwest-vergent thrusting by the YXL thrust system produces the lower SZG anticline (the SZG wedge structure), the northwestern SZG-YSS anticline and surface deformations.

The SE SZG-YSS anticline strikes southeast (Figure 1). Its SW limb dips to the southwest at ~50°–80° decreasing southeastward, but overturns somewhere, and is cut by a thrust (Xu et al., 2018b). The seismic profile (Figure 7b) images the limb poorly. Its crest consists of sub-horizontal reflectors, agreeing with surface geology observations. The region of homogeneous dip between the axial surfaces A and A'' defines the NE limb dipping to the northeast at~21°, in agreement with surface geology observations. The width of this region of homogeneous dip maintains constant in the pregrowth strata. This region narrows upward along the growth axial surface G. The axial surface A'' splits upward into the growth axial surface G and G1. The crest of the anticline is the region of homogeneous dip between the axial surfaces B and A', merging downwards to form the axial surface AB extending downward to the SZG ramp. We suppose the structural interpretation that the SE SZG-YSS anticline is a forelimb breakthrough fault-propagation fold anticline (Figure 7b) according to locating of regions of homogeneous dip and the growth fault-propagation folding theory (Suppe and Medwedeff, 1990; Suppe et al., 1992).

Appendix B: The GCG anticline and its related fault

The GCG anticline is in the middle of the YXL anticlinorium, plunging to the southeast (Figure 1). The SW limb of the anticline dips to the southwest at ~35°, and the NE limb dips northeast at ~25° (Figure 5b). Dip angles of both limbs lower toward the southeast. The horizontal region of homogeneous dip between the axial surfaces A and D' corresponds to the syncline between the SZG-YSS and the GCG anticlines (Figures 5a and 5b). The SW limb of the anticline is made up of the ~28°-southwest-dipping and ~4.9-km-long region of homogeneous dip. This region extends upward to the ground surface and downward to the GCG flat. The horizontal region of homogeneous dip terminating downward at the GCG flat between D and E' consists of the crest of the anticline. The region of homogeneous dip between the axial surfaces E and E' dips to the northeast at ~11° and have a width of ~5.4 km, consisting of the NE limb. The region extends upward to the ground surface and downward to the GCG ramp. The horizontal region of homogeneous dip between the axial surface E and F' is composed of a syncline between the GCG and the XSQ-YQZ anticlines. On basis of above-mentioned locating regions of homogeneous dip, we interpret GCG as a classic fault-bend fold anticline (Figure 5b).

Appendix C: The XSQ-YQZ anticline and its related fault

The XSQ-YQZ anticline is the northeastern part of the YXL anticlinorium (Figure 1). Its middle segment plunges (Figure 1). The SW limb dips to the southwest at a high angle; the NE limb dips to the northeast at a lower angle, but changes significantly. Figure 5b shows that the anticline consists of four regions of homogeneous dip. The horizontal region of homogeneous dip between the axial surfaces E and F' represents the syncline between the XSQ-YQZ and the GCG anticlines, narrowing upward and widening downward until the GCG flat. The axial surface F' serves as the synclinal axial one of the SW limb. The region of homogeneous dip between the axial surfaces F and F' maintains a constant width and dips to the southwest at ~20° to form the SW limb of the anticline. The region of the homogeneous dip between the axial surfaces F and H' dips to the northeast at ~7.5° and widens upward from the upper XSQ ramp to form the crest of the anticline. The region of homogeneous dip between the axial surfaces F and H' dips northeast at ~20°. The seismic profile 4 km northwest of Figure 5a shows that this region turns into being horizontal. So, we deduce the existence of the axial surface H, and that the width between the axial surfaces H and H' is the minimum. There exist sub-horizontal reflectors below this region of homogeneous dip, which form a disharmony. According to locating regions of homogeneous dip in the seismic profile (Figures 5a and 5b), we interpret the XSQ-YQZ as a multi-fault bend fold anticline.

Appendix D: The Shaxi wedge structure

The buried Shaxi structure is revealed by seismic exploration. It is well imaged as a monocline consisting of a kink band between the axial surface M, M' and Gs, and the horizontal regions of homogeneous dip in its both sides (Figures 5b and 6b). The kind band between the axial surface Gs and M, above the middle member of the Xiaganchaigou Formation, narrows upward and fades away in the middle part of the Shangyousha Shan Formation. It maintains a constant width between the axial surfaces M and M' and extends to ~ 3.5 s in time-depth. Based on locating regions of homogeneous dip (Figure 5b and 6b), we interpret Shaxi as a wedge structure.

Acknowledgment

This study benefited from discussions with Profs. Zhaojie Guo, Zhouchuan Huang, and Tao Wang. This study was supported by the National Natural Science Foundation of China (grants 41672198 and 41372201), the National Key R&D Plan (Grant No. 2017YFC0601402), and the Major National R&D Projects Programs of China (2016ZX05003-006). LABEX VOLTAIRE (ANR-10-LABX-100-01), and EQUIPEX PLANET (ANR-11-EQPX-0036) are appreciated. The foucs parameters of the March 28, 2019 Mw 5.04 Mangya earthquake and aftershorks from China Earthquake Data Center website presented in this manuscript can be found online via Mendley (https://www.mendeley.com/) at http://dx.doi.org/10.17632/npbw484bgf.1.

References

Bian, Q., Zhang, D., Yu, X., Cheng, X., Du, W., Liu, R., Wang, Z. and Guo, Z., 2019, Transpressional salt tectonic system in western Qaidam Basin, Western China, AAPG Bulletin, v. 103, no. 3, 547–568, doi:10.1306/08161817119.

Chang, H., Li, L., Qiang, X., Garzione, C. N., Pullen, A., An, Z., 2015, Magnetostratigraphy of Cenozoic deposits in the western Qaidam Basin and its implication for the surface uplift of the northeastern margin of the Tibetan Plateau, Earth and Planetary Science Letters, 430, 271–283, http://dx.doi.org/10.1016/j.epsl.2015.08.029

Cheng, X., D. Zhang, M. Jolivet, X. Yu, W. Du, R. Liu, and Z. Guo, 2018, Cenozoic structural inversion from transtension to transpression in Yingxiong Range, western Qaidam Basin: New insights into strike-slip superimposition controlled by Altyn Tagh and Eastern Kunlun Faults: Tectonophysics, v. 723, p. 229–241, doi:10.1016/j.tecto.2017.12.019.

Chen Y., V. Courtillot, J.P. Cogné, J. Besse, Z. Yang and R. Enkin, 1993, The configuration of Asia prior to the collision of India: Cretaceous paleomagnetic constraints, Journal of Geophysical Research, 98, 21, 927 – 21,941.

Chen Y., S. Gilder, N. Halim, J.-P. Cogné, and V. Courtillot, 2002, New Mesozoic and Cenozoic data help constrain the age of motion on the Altyn Tagh fault and rotation of the Qaidam basin, Tectonics, doi: 10.1029/2001TC901030.

Cheng, F., Garzione, C. N., Jolivet, M., Guo, Z., Zhang, D., Zhang, C., & Zhang, Q. (2019). Initial deformation of the northern Tibetan Plateau: Insights from deposition of the Lulehe Formation in the Qaidam Basin. Tectonics, 38. https://doi.org/10.1029/2018TC005214.

Chen, X.H., Dang, Y.Q., Yin, A., et al., 2010, The Basin-mountain Coupling and Evolution of Qaidam Basin and Its Surrounding Mountains, Beijing: Geological Publishing House, 1-437. (in Chinese).

China Earthquake Data Center, 2019, http://data.earthquake.cn

Feng, G., Hetland, E. A., Ding, X., Li, Z., Zhang, L.,2010, Coseismic fault slip of the 2008 Mw 7.9 Wenchuan earthquake estimated from InSAR and GPS measurements, Geophysical Research Letters, v. 37, L01302, doi:10.1029/2009GL041213.

Huang, H., Huang, Q., and Ma, Y., 1996, Geology of Qaidam Basin and its petroleum prediction: Beijing, Geological Publishing House, 257 p.

Horton, B.K., 2012, Cenozoic evolution of hinterland basins in the Andes and Tibet, IN: Busby and A. Azor, 2012, Tectonics of sedimentary basins: Recent Advances, John Wiley & Sons, Ltd, West Sussex, PO19 8SQ, UK.

Huo, G.M., ed., 1990, Petroleum geology of China: Oil fields in Qinghai and Xizang: Chinese Petroleum Industry Press, v. 14, 483 p.

Hubert-Ferrari, A., Suppe, J., Gonzalez-Mieres, R. and Wang, X., 2007, Mechanisms of active folding of the landscape (southern Tian Shan, China), Journal of Geophysical Research, v. 112, B03S09, doi: 10.1029/2006JB004362

Huang, K., Chen, L., Xiao, A., Shen, Y., Cenozoic Deformation Characteristics of the Xianshuiquan Anticline in the Northwestern Qaidam Basin and Its Significance, Geological Journal of China Universities, V. 24, No.5, 761-768. (In Chinese with English abstract)

Liu-Zeng, J., Zhang, Z., Wen, L., Tapponnier, P., Sun, J., Xing, X., Hu, G., Xu, Q., Zeng, L., Ding, L., Ji, C., Hudnut, K.W., van der Woerd, J., Co-seismic ruptures of the 12 May 2008, Ms 8.0 Wenchuan earthquake, Sichuan: East–west crustal shortening on oblique, parallel thrusts along the eastern edge of Tibet, Earth and Planetary Science Letters, v. 286 , 355–370, doi:10.1016/j.epsl.2009.07.017.

Molnar, P. and Tapponnier, P., 1975, Cenozoic tectonics of Asia: Effects of continental collision, Science, 189,419-426.

Mueller, K., Suppe, J., 1997, Growth of Wheeler Ridge anticline, California: geomorphic evidence for fault-bend folding behaviour during earthquakes, Journal of Structural Geology, v. 19, issues 3-4, 383-396, https://doi.org/10.1016/S0191-8141(96)00112-5

Medwedeff, D. A., 1989, Growth fault-bend folding at southeast Lost Hills, San Joaquin Valley, California: AAPG Bulletin, v. 73, p. 54–67.

Medwedeff, D. A. and J. Suppe, 1997, Multibend fault-bend folding: Journal of Structural Geology, 19, p. 279–292.

Pang, J., Yu, J., Zheng, D., Wang, W., Ma, Y., Wang, Y., et al. 2019. Neogene expansion of the Qilian Shan, north Tibet: Implications for the dynamic evolution of the Tibetan Plateau. Tectonics, 38, 1018–1032. https://doi.org/10.1029/2018TC005258

Pan JW, Li HB, Sun ZM, Liu DL, Wu C and Yu CQ. 2015. Tectonic responses in the Qaidam basin induced by Cenozoic activities of the Altyn Tagh fault. Acta Petrologica Sinica, 31(12): 3701-3712 (in Chinese with English abstract)

Qinghai BGMR (Qinghai Bureau of Geology and Mineral Resources), 1991, Regional geology of Qinghai Province: Beijing, Geological Publishing House.

Qiu, N., 2002, Tectono-thermal evolution of the Qaidam Basin, China: Evidence from Ro and apatite fission track data: Petroleum Geoscience, v. 8, p. 279–285.

Rieser, A.B., Liu, Y.J., Genser, J., Neubauer, F., Handler, R., Friedl, G., and Ge, X.H., 2006a, 40Ar/39Ar ages of detrital white mica constrain the Cenozoic development of the intracontinental Qaidam Basin: Geological Society of America Bulletin, v. 118, p. 1522–1534, doi: 10.1130/B25962.1.

Rieser, A.B., Liu, Y.J., Genser, J., Neubauer, F., Handler, R., and Ge, X.H., 2006b, Uniform Permian 40Ar/39Ar detrital mica ages in the eastern Qaidam Basin (NW China): Where is the source?: Terra Nova, v. 18, p. 79–87, doi: 10.1111/j.1365-3121.2005.00666.x.

Song, T., and Wang, X., 1993, Structural styles and stratigraphic patterns of syndepositional faults in a contractional setting: Examples from Qaidam basin, northwestern China: AAPG Bulletin, v. 77, p. 102–117.

Sun, Z.M., Yang, Z.Y., Pei, J.L., Ge, X.H., Wang, X.S., Yang, T.S., Li, W.M., and Yuan, S.H., 2005, Magnetostratigraphy of Paleogene sediments from northern Qaidam basin, China: Implications for tectonic uplift and block rotation in northern Tibetan plateau: Earth and Planetary Science Letters, v. 237, p. 635–646, doi: 10.1016/j.epsl.2005.07.007.

Suppe, J., 1983, Geometry and Kinematics of fault-bend folding, American Journal of Science, 283, 684-721.

Suppe, J. and Medwedeff ,1990, Geometry and Kinematics of fault-propagation folding, Eclogae Geologicae Helvetiae, 83

Suppe, J.S., Chou, G.T., and Hook, S.C. (1992) Rates of folding and faulting determined from growth strata. In McClay, K.R. (ed.), Thrust Tectonics, pp. 105–122. Chapman and Hall, London.

Suppe, J., Sabat, F., Muñoz, J.A., Poblet, J., Roca, E., and Vergés, J. (1997) Bed-by-bed fold growth by kink-band migration: Sant Llorenc de Morunys, Eastern Pyrenees. Journal of Structural Geology, 19, 443–461.

Tapponnier, P. and Molnar P., 1976, Slip-line field theory and large-scale continental tectonics, Nature, 264 (5584): 319~ 324.

Tapponnier, P. and Molnar, P., 1977, Active faulting and tectonics in China, Journal of Geophysics Research, 82(20), 2905–2930, doi: 10.1029/JB082i020p02905.

Tapponnier, P. and Molnar, P., 1979, Active faulting and Cenozoic tectonics of the Tien Shan, Mongolia, and Baykal regions, Journal of Geophysical Research, v. 84, no. B7, 3425-3459.

Tapponnier, P, Peltzer, G., Le Dain, A. Y., Armijo, R., Cobbold P., 1982, Propagating extrusion tectonics in Asia: New insight s from simple experiments with plasticine, Geology, 10: 611 ~ 616.

Tapponnier, P, Xu, Z.Q., Roger, F., Meyer, B., Arnaud, N., Wittlinger, G., Yang, J.S., 2001, Oblique stepwise rise and growth of the Tibet plateau, Science, 294, 1671-1677, DOI: 10.1126/science.105978

USGS (U.S. Geological Survey), 2019, https://earthquake.usgs.gov/earthquakes/eventpage/us2000k66p/executive

Wang, S., Wu, G., Shi, Z., 1999, Catalogue of Chinese Earthquakes (1912–1990, MS ≥4.7), Beijing: China Science and Technology Press.

Wang, C., Dai, J., Zhao, X., Li, Y., Grahamd, S. A., He, D., Ran, B., Meng, J., 2014, Outward-growth of the Tibetan Plateau during the Cenozoic: A review, Tectonophysics, 621, 1–43, http://dx.doi.org/10.1016/j.tecto.2014.01.036.

Wang, W., Qiao, X., Yang, S., Wang, D., 2017a, Present-day velocity field and block kinematics of Tibetan Plateau from GPS measurements, Geophysical Journal International, 208, 1088–1102, doi: 10.1093/gji/ggw445.

Wang, W., Zheng, W., Zhang, P., Li, Q., Kirby, E., Yuan, D., Zheng, D., Liu, C., Wang, Z., Zhang, H. & Pang, J., 2017b, Expansion of the Tibetan Plateau during the Neogene. Nat. Commun. 8, 15887 doi: 10.1038/ncomms15887.

Wells, D. L., and K. J. Coppersmith, 1994, New empirical relationships among magnitude, rupture length, rupture width, rupture area, and surface displacement, Bull. Seismol. Soc. Am., 84, 974-1002.

Wu C., Yan C.F., Li H.B., Tian G.R., Sun Z.M., Liu D.L., Yu C.Q. and Pan J.W., 2013, Cenozoic tectonic evolution of the western Qaidam Basin and its constrain on the growth of the northern Tibetan Plateau. Acta Petrologica Sinica, 29(6): 2211–2222

Wu, W., Yuan, J., Wang, J., Shi, Y., Chen, Y., Zou, K., Jia, D., 2020, A Late Neogene framework and transpressional system within the Yingxiongling Range, western Qaidam Basin, Northeast Tibetan Plateau: Insights from seismic reflection profiles and active tectonics, Journal of Asian Earth Sciences, DOI: https://doi.org/10.1016/j.jseaes.2019.104061

Xia, W., Zhang, N., Yuan, X., Fan, L., and Zhang, B., 2001, Cenozoic Qaidam basin, China: A stronger tectonic inversed, extensional rifted basin: AAPG Bulletin, v. 85, p. 715–736.

Xu, C., Liu, Y., Wen, Y., Wen, Y., Wang, R.-Q., 2010, Coseismic Slip Distribution of the 2008 Mw 7.9 Wenchuan Earthquake from Joint Inversion of GPS and InSAR Data, Bulletin of the Seismological Society of America, 100(5B): 2736-2749, DOI: 10.1785/0120090253.

Xu, J., Hui, X., Cheng, H., Zhang, X., Shang, S., 2108a, Analysis on Late Quaternary Tectonic Deformation of the Shizigou Fault, Southwestern Margin of the Qaidam Basin, Journal of Seismological Research, v.41, no.1, 46-54. (In Chinese with English abstract)

Xu, J., Hui, X., Cheng, H., Zhang, X., Shang, S., 2108b, Paleoseismology and late Quaternary slip rate of the Youshashan fault at southern margin of Qaidam basin, Seismology and Geology, v.40, no.2, 465-479, doi: 10.3969 /j.issn.0253-4967.2018.02.013. (In Chinese with English abstract)

Xu, X., Wen, X., Yu, G., Chen, G., Klinger, Y., Hubbard, J., and Shaw, J., 2009, Coseismic reverse- and oblique-slip surface faulting generated by the 2008 Mw 7.9 Wenchuan earthquake, China, Geology, 37 (6): 515–518, https://doi.org/10.1130/G25462A.1.

Yang, F., Ma, Z., Xu, T., and Ye, S., 1992, A Tertiary paleomagnetic stratigraphic profile in Qaidam basin: Acta Petrologica Sinica, v. 13, p. 97–101.

Yin, A. & Harrison, T.M. (2000) Geologic evolution of the Himalayan Tibetan Orogen. Annu. Rev. Earth Planet. Sci. 28, 211–80.

Yin, A., P. Rumelhart, R. Butler, E. Cowgill, T. Harrison, D. Foster, R. Ingersoll, Q. Zhang, X.-Q. Zhang, and X.-F. Wang, 2002, Tectonic history of the Altyn Tagh fault system in northern Tibet inferred from Cenozoic sedimentation: Geological Society of America Bulletin, v. 114, no. 10, p. 1257–1295, doi:10.1130/0016-7606(2002)114<1257:THOTAT>2.0.CO;2.

Yin, A., Dang, Y., Zhang, M., McRivette, M.W., Burgess, W.P., and Chen, X., 2007, Cenozoic tectonic evolution of Qaidam basin and its surrounding regions (part 2): Wedge tectonics in southern Qaidam basin and the Eastern Kunlun Range, in Sears, J.W., Harms, T.A., and Evenchick, C.A., eds., Whence the Mountains? Inquiries into the Evolution of Orogenic Systems: A Volume in Honor of Raymond A. Price: Geological Society of America Special Paper 433, p. 369–390, doi: 10.1130/2007.2433(18).

Yin, A., Dang, Y.-Q., Wang, L.-C., Jiang, W.-M., Zhou, S.-P., Chen, X.-H., Gehrels, G.E., and McRivette, M.W., 2008a, Cenozoic tectonic evolution of Qaidam Basin and its surrounding regions (part 1): The southern Qilian Shan–Nan Shan thrust belt and northern Qaidam Basin: Geological Society of America Bulletin, v. 120, no. 7–8, p. 813–846, https://doi .org /10 .1130 /B26180 .1.

Yin, A., Dang, Y.Q., Zhang, M., Chen, X.H., and McRivette, M.W., 2008b, Cenozoic tectonic evolution of the Qaidam Basin and its surrounding regions (Part 3): Structural geology, sedimentation, and regional tectonic reconstruction: Geological Society of America Bulletin, v. 120, no. 7–8, p. 847–876, https://doi.org /10.1130 /B26232.1.

Yu, F., Y. Wang, X. Li, X. Li, and Z. Feng, 2011, Deformation characteristics and genesis simulation of the Shizigou-Youshashan structural belt in Qaidamu Basin: Geotectonica et Metallogenia, v. 2, p. 6.

Zhou, J., F. Xu, T. Wang, A. Cao, and C. Yin, 2006, Cenozoic deformation history of the Qaidam Basin, NW China: Results from cross-section restoration and implications for Qinghai–Tibet Plateau tectonics: Earth and Planetary Science Letters, v. 243, no. 1–2, p. 195–210, doi: 10.1016/j.epsl.2005.11.033.

Zuza, A.V., Wu, C., Wang, Z., Levy, D. A., Li, B., Xiong, X., and Chen, X., 2019, Underthrusting and duplexing beneath the northern Tibetan Plateau and the evolution of the Himalayan-Tibetan orogen, LITHOSPHERE; v. 11; no. 2; p. 209–231, https://doi.org/10.1130/L1042.1

Table 1. Cenozoic stratigraphy of the YXL region, southwestern Qaidam Basin. Simplified from Bian et al. (2019).

Formation	Age (Ma)	Symbol	Lithology
Qigequan	2.5	Q_1q	Gray, grayish yellow conglomerate, pebbled sandstone, gray, grayish white sandy mudstone.
Shizigou	8.1	N_2^3s	Upper member: grayish white, brown mudstone, and interlayered siltstone. Lower member: pebbled sandstone, siltstone, argillaceous siltstone, and mudstone.
Shangyousha Shan	15.3	N_2^2sy	Gray, dark gray mudstone intercalated with dark gray calcareous mudstone.
Xiayousha Shan	20	N_2^1xy	Upper member: thick gray mudstone intercalated with marlstone and limestone. Lower member: gray mudstone intercalated with thin marlstone and siltstone.
Shangganchaigou	35.5	N_1sg	Gray mudstone intercalated with siltstone.
Upper Xiaganchaigou	37.8	E_3^2xg	Evaporate, gray mudstone, and calcareous mudstone intercalated with argillaceous siltstone.
Lower Xiaganchaigou	43.8	E_3^1xg	Brown mudstone and interlayered fine-grained sandstone.
Lulehe		$E_{1-2}l$	Upper member: mudstone interlayered with siltstone. Lower member: conglomerate.

Table 2. Logging of boreholes H6-2-510 from the depth of 1970 m to 1990 m, and H4-2-506 from the depth of 1920 m to 2014 m.

Borehole name	**Starting depth (m)**	**Ending depth (mm)**	**Thickness (m)**	**Normal inner diameter (mm)**	**Maximum inner diameter (mm)**	**Minimum inner diameter (mm)**	**Maximum radius (mm)**	**Minimum radius(mm)**	**Deformation amount (mm)**
H6-2-510	1970.0	1990.0	20	247.91	254.86	172.88	128.12	47.60	75.03
H4-2-506	1920.0	1923.0	3.0	247.91	255.08	199.51	129.21	79.54	48.40
	1991.0	1997.0	6.0	247.91	259.19	245.75	131.64	119.61	2.16
	1997.0	2014.0	17.0	247.91	255.36	217.96	128.75	104.75	29.95

Table 3. Coseismic slips of the Mangya earthquake fault at the eight borehole sites.

Borehole name	Latitude	Longitude	Depth of damage (m)	Offset (mm)
H4-3-414	38°18′09"	90°55′25"	~2034.8	400 ± 13
H4-3-510	38°18′18"	90°55′28"	~2110.5	400 ± 13
H4	38°18′01"	90°55′18"	~1700.0	107 ± 42
H6-2-510	38°18′50"	90°55′06"	~1994.7	182 ± 58
H4-2-506	38°18′57"	90°54′50"	~1925.0	28 ± 21
H2-3-413	38°16′24"	90°54′49"	~1500.0	188 ± 59
H4-3-411	38°16′58"	90°54′21"	~2159.0	188 ± 59
H4-2-510	38°17′36"	90°54′05"	~2271.0	107 ± 42

Table 4. The focal mechanism solution of the March 28, 2019 Mw 5.04 Mangya Earthquake.

Solution	Strike (°)	Dip (°)	Slip angle (°)
Plane 1	302.4	20.2	134.0
Plane 2	76.5	75.6	75.7

Figure 1. (a) Simplified geological map of Yingxiong Ling (YXL), southwestern Qaidam. Lower-hemisphere focal mechanisms of the March 28, 2019 Mw 5.04 Mangya earthquake shows compressional quadrants in blue and dilational quadrants in clear. Locations of seismic profiles, Figures 2, 8, and 12 are marked. (b) Shaded relief map showing major faults and topographic features of the Himalayan-Tibetan orogen. The black rectangular marks the location of Figure 1a. Fault traces are from Yin & Harrison (2000) and Tapponnier et al. (2001). WS, Western Himalayan Syntaxis; ES, Eastern Himalayan Syntaxis; MMT, Main Mantle Thrust; AKMS, Ayimaqing–Kunlun–Mutztagh suture; JS, Jinsha suture; BNS, Bangonghu–Nujiang suture; IZS, Indus–Zangbo suture.

Figure 2. Coseismic slip contour map of the Shizigou (SZG) ramp on the March 28, 2019 Mw 5.04 Mangya earthquake in Yingxiong Ling. Eight damaged boreholes define the coseismic underground rupture area of the event. Epicenters of the mainshock and aftershocks (See Table S1) are from China Earthquake Data Center (2019).

Figure 3. The offset drilling rod of borehole H4-3-414 showing that the low-angle SZG ramp cut it just at the faulting moment, and its possible fracturing process. See Figure 2 for the borehole location. Photo (a) was shot when the pipe was pulled out from the hole, and photo (b) was shot when the pipe was laid down. The outer diameter of the drill pipe is 101.6 mm. (c) Configuration of the borehole structure before being offset. (d) The casing pipe is sheared, as the right side of the upper casing pipe just touches the right side of the drilling rod. (e) With the offset increasing, the left side of the lower casing pipe just touches the left side of the drilling rod. (f) The drilling rod near the fault plane is flattened. (g) The flattened drilling rod is bend like a kink and pulled cut. Assuming that the kink-like deformation of the drilling pipe rod is symmetrical relative to the broken surface and the pipe is just broken away, the offset is 400 ± 13 mm.

Figure 4. Photos of the lead seal before being put into (a and b) and after being pulled out (c and d) from borehole H4-3-414. The diameter of the lead seal bottom is 165 mm and the inner diameter of the casing pipe is 166.63 mm. The side face of the lead seal has scratches, but no imprint exists in its bottom surface, revealing that the coseismic slip at this borehole site is more than 196.85 mm, the outer diameter of the casing pipe.

Figure 5. Clear (a) and interpreted seismic profiles (b) crossing the middle segment of the YXL anticlinorium. The rightmost segment separated from the main part is located to about 4 km northwest of the main part. See Figure 1 for the location. LSZGA, the lower Shizigou anticline; SZGR, the Shizigou ramp; SZGBR, the Shizigou back-ramp; SZGF, the Shizigou flat; LSZGR, the lower Shizigou ramp; GCGF, the Ganchaigou flat; GCGR, the Ganchaigou ramp; XSQF, the Xianshuiquan flat; UXSQR, the upper Xianshuiquan ramp; LXSQR, the lower Xianshuiquan ramp; LXSQF, the lower Xianshuiquan Flat.

Figure 6. Clear (a) and interpreted seismic profiles (b) crossing the northwestern SZG-YSS anticline. See Figures 1 and 2for the location. The green line denotes the coseismic rupture segment of the SZG ramp on the March 28, 2019 Mw 5.04 Mangya earthquake. The vertical scale is equal to the horizontal one. LSZGA, the lower Shizigou anticline; SZGR, the Shizigou ramp; SZGBR, the Shizigou back-ramp; SZGF, the Shizigou flat;

LSZGR, the lower Shizigou ramp; GCGF, the Ganchaigou flat. Symbols are the same as in Figures 5

Figure 7. Clear (a) and interpreted seismic profiles (b) crossing the southeastern SZG-YSS anticline. The vertical scale is equal to the horizontal one. See Figure 1 for the location. Symbols are the same as in Figures 5 and 6. YSSR, the Youshan Shan ramp.

Figure 8. The folded topographic surface and a fault scarp along the southwestern edge of northwestern YXL. The red solid line with bars toward the upper plate marks the SZG ramp trace; the red dashed line marks the trace of the active axial surface B'. See the location in Figure 1. The satellite image is sourced from Google Earth.

Figure 9. An outcrop photo of deformed alluviums by the SZG ramp (a) and its interpretation (b). Folding of Unit A and Unit B1 represents two thrusting events rupturing the ground surface. The event A happened between 39.77 ± 6.38 ka and 32.63 ± 2.27 ka, and event B1 at 6.16 ± 0.52 ka (ages after Xu et al., 2018a). See the location in Figure 8.

Figure 10. The folded topographic surface and the fault scarp along the southwestern edge of northwestern YXL. (a) A photo of the fold and the fault scarps. (b) A topographic profile crossing the southwestern edge of YXL. The right side of the photo points to the northwestern SZG-YSS anticline. The two topographic inflection points correspond to the outcrop of the SZG ramp and the axial surface of B', respectively. See the location in Figure 8.

Figure 11. (a) A trench photo of the folded sediments produced by southwest-vergent thrusting of the lower SZG wedge structure. See location in Figure 8. (b) Reinterpretation of the trench. Folded Ug1 and Ug2 represent two thrusting events. (c) A simplified model of a terraced hillslope formed on the front limb of a buried wedge thrust structure (modified from Mueller and Suppe, 1997). Folding events occur at times Tn, defined by onlapped sediment packages. Terraces were developed above the sediments deposited above the strata that had already been folded through an active axial surface. Limb widening by each event is denoted by Xn, which is measured parallel to bedding between outer terrace edges.

Figure 12. The fold scarp along the northeastern edge of YXL. See the location in Figure 1. The Qigequan Formation in the southwest of the scarp is leveled, and patchily covered by evaporites and active dunes; the playa to the northeast of the scarp is locally covered by alluviums and debris avalanches. The dashed line marks the trace of the active axial surface H. Figures 13 a, b, c and d are marked. The satellite image is sourced from Google Earth.

Figure 13. Photos and growth models of the scarp along the northeastern edge of YXL. See Figure 12 for the locations of the topographic profiles and the viewpoints of the photos. (a) A horizontally-flipped photo of the scarp at the mouth of the hiking stream. (b) A topographic profile crossing the scarp close to the hiking stream. This profile shows that the scarp height at this site is ~31 m. (c) A photo of the scarp along the pipe stream.

The left end of the photo shows that the recent alluviums cover the northeast-dipping limb of the XSQ-YQZ anticline to form a classic growth unconformity. The angles of the folded alluviums become lower northeastwards and contact with the sediments below them in unconformity, disconformity, and conformity. (d) A topographic profile crossing the scarp near the pipe stream. This profile shows that the scarp is ~30 m high at this site. (e) A dimensionless wide hinge zone model for changing horizon shape with increasing fractional displacement through a hinge zone with a total change in a dip of 56° (from Hubert-Ferrari et al., 2007). (f) Dimensionless templates of fold shapes for incrementally increasing displacement through the hinge. The hinge zone is bounded by the entry and exit axial surfaces with an arbitrary width of *w* (from Hubert-Ferrari et al., 2007).

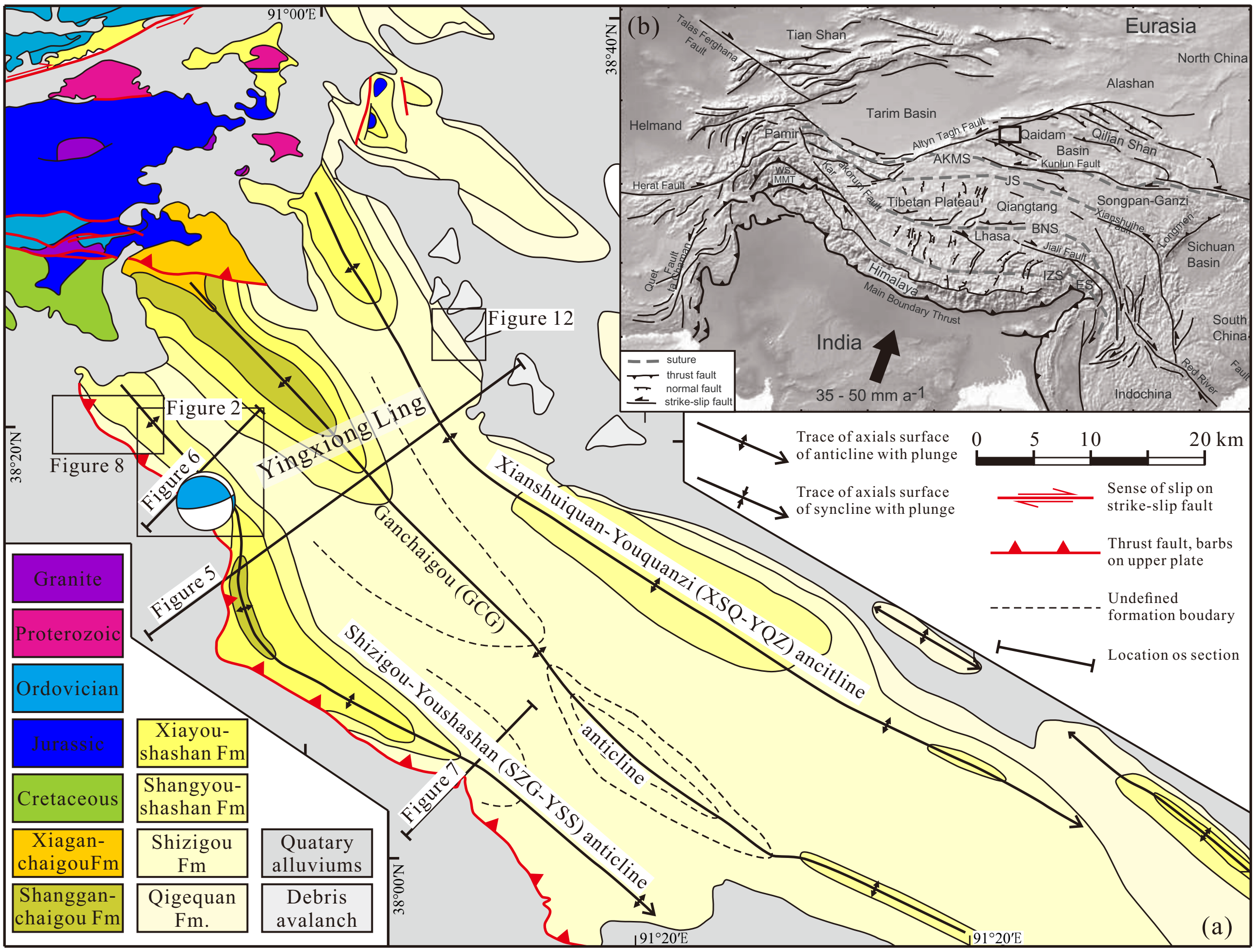

Figure 1. (a)Simplified geological map of Yingxiong Ling, southwestern Qaidam. Lower-hemisphere focal mechanisms of the March 28, 2019 Mw 5.04 Manya earthquake shows compressional quadrants in blue and dilational quadrants in clear. Locations of seismic profiles, Figures 2, 8 and 12 are marked. (b) Shaded relief map showing major fault and topographic features of the Himalayan-Tibetan orogen. The black rectangular marks the location of Figure 1a in the Himalayan-Tibetan collision system. Fault traces are from Yin & Harrison (2000), Tapponnier et al. (2001). WS, Western Himalayan Syntaxis; ES, Eastern Himalayan Syntaxis; MMT, Main Mantle Thrust; AKMS, Ayimaqin–Kunlun–Mutztagh suture; JS, Jinsha suture; BNS, Bangong–Nujiang suture; IZS, Indus–Zangbo suture.

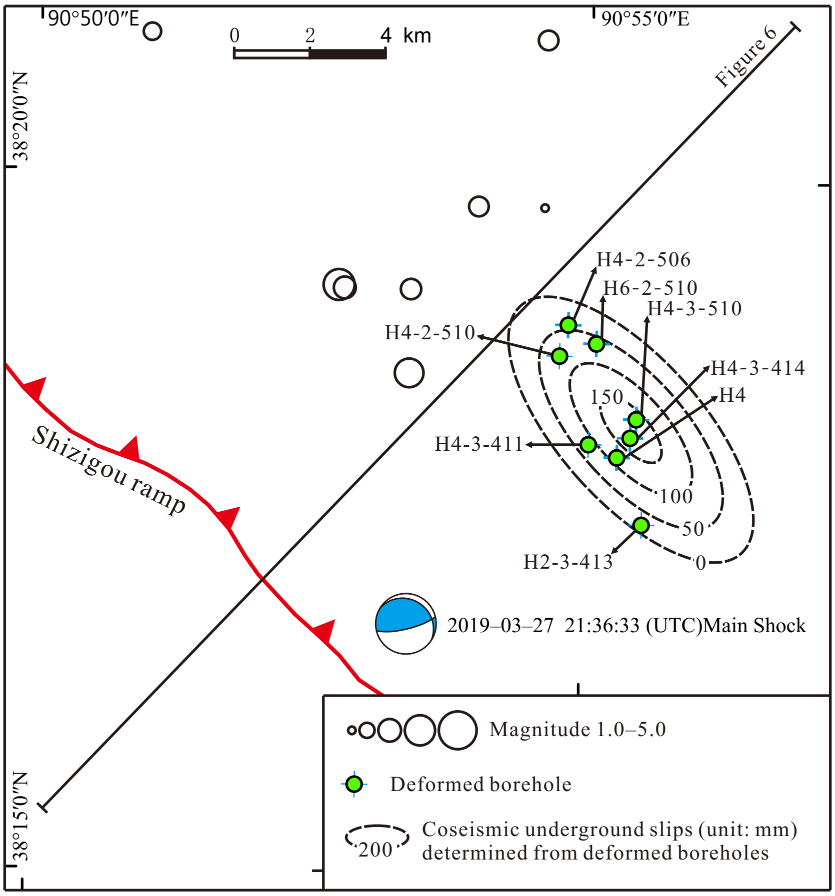

Figure 2. Coseismic slip contour map of the Shizigou (SZG) ramp on the March 28, 2019 Mw 5.04 Mangya earthquake in Yingxiong Ling. Eight damaged boreholes define the coseismic underground rupture area of the event. Epicenters of the main shock and aftershocks are from China Earthquake Data Center (2019).

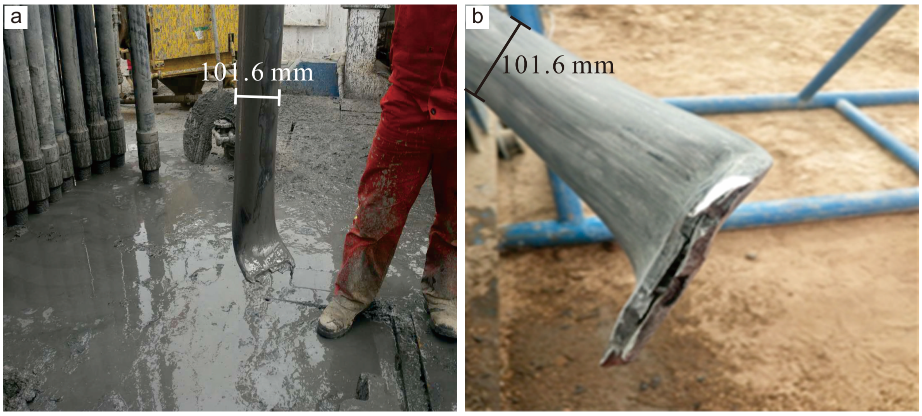

Figure 3. The offset drilling rod of borehole Shi41H4-3-414 showing that the low-angle SZG ramp cut it just at the faulting moment. Photo (a) was shot when the pipe was pulled out from the hole, and photo (b) was shot when the pipe was laid flat. The diameter of the drill pipe is 101.6 mm. See Figure 2 for the location of the borehole.

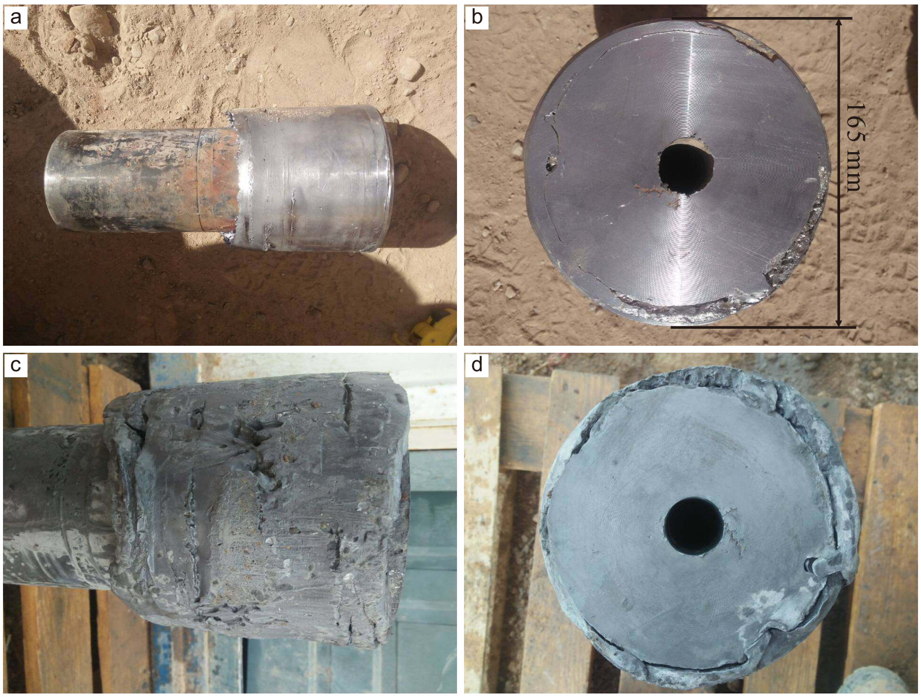

Figure 4. Photos of the lead seal before (a and b) being put into and after (c and d) being pulled out from borehole Shi41H4-3-414. The diameter of the lead seal is 165 mm and the inner diameter of the casing pipe is 172.05 mm. The side face of the lead seal has scratches, but no imprint exists in its bottom surface, which reveals that the coseismic slip at this borehole site is more than the casing pipe diameter of 196.85 mm.

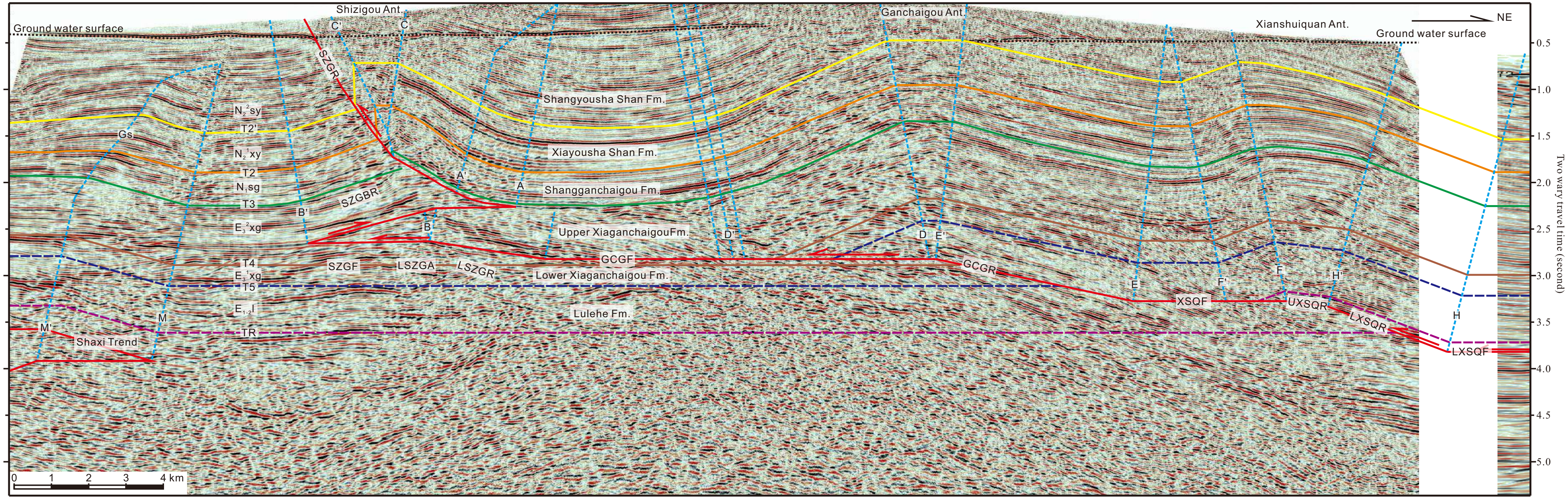

Figure 5. Interpreted seismic profile crossing the middle segment of the YXL anticlinorium. See Figure 1 for location. LSZGA, the lower Shizigou anticline; SZGR, the Shizigou ramp; SZGBR, the Shizigou back-ramp; SZGF, the Shizigou flat; LSZGR, the lower Shizigou ramp; GCGF, the Ganchaigou flat; GCGR, the Ganchaigou ramp; XSQF, the Xianshuiquan flat; UXSQR, the upper Xianshuiquan ramp; LXSQR, the lower Xianshuiquan ramp; LXSQF, the lower Xianshuiquan Flat.

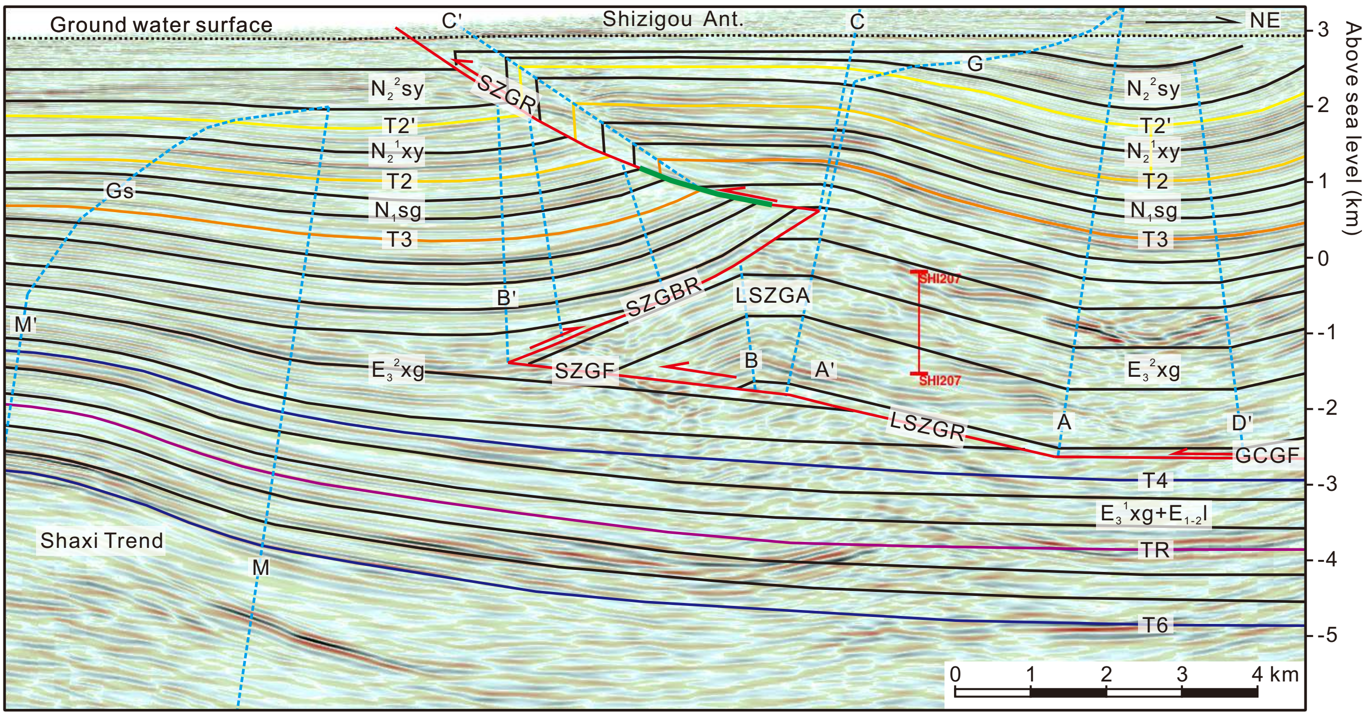

Figure 6. Interpreted seismic crossing the western SZG-YSS anticline. The green line segment on the SZG ramp is the coseismic rupture of the March 28, 2019 Mw 5.04 Mangya earthquake. The vertical scale is equal to the horizontal one. See Figure 1 for location. LSZGA, the lower Shizigou anticline; SZGR, the Shizigou ramp; SZGBR, the Shizigou back-ramp; SZGF, the Shizigou flat; L SZGR, the lower Shizigou ramp; GCGF, the Ganchaigou flat.

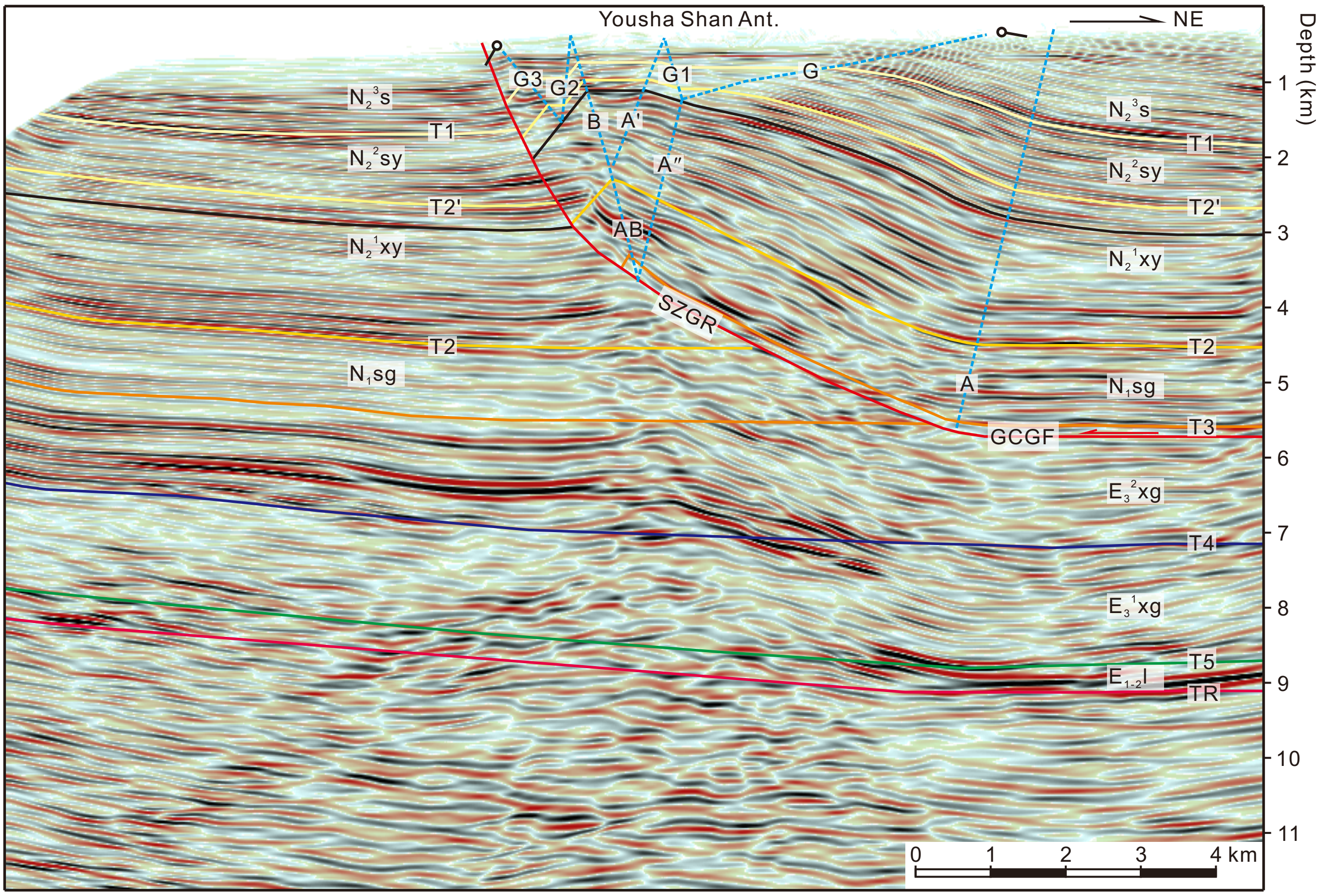

Figure 7. Interpreted seismic profile crossing the eastern segment of the SZG-YSS anticline. The vertical scale is equal to the horizontal one. See Figure 1 for location.

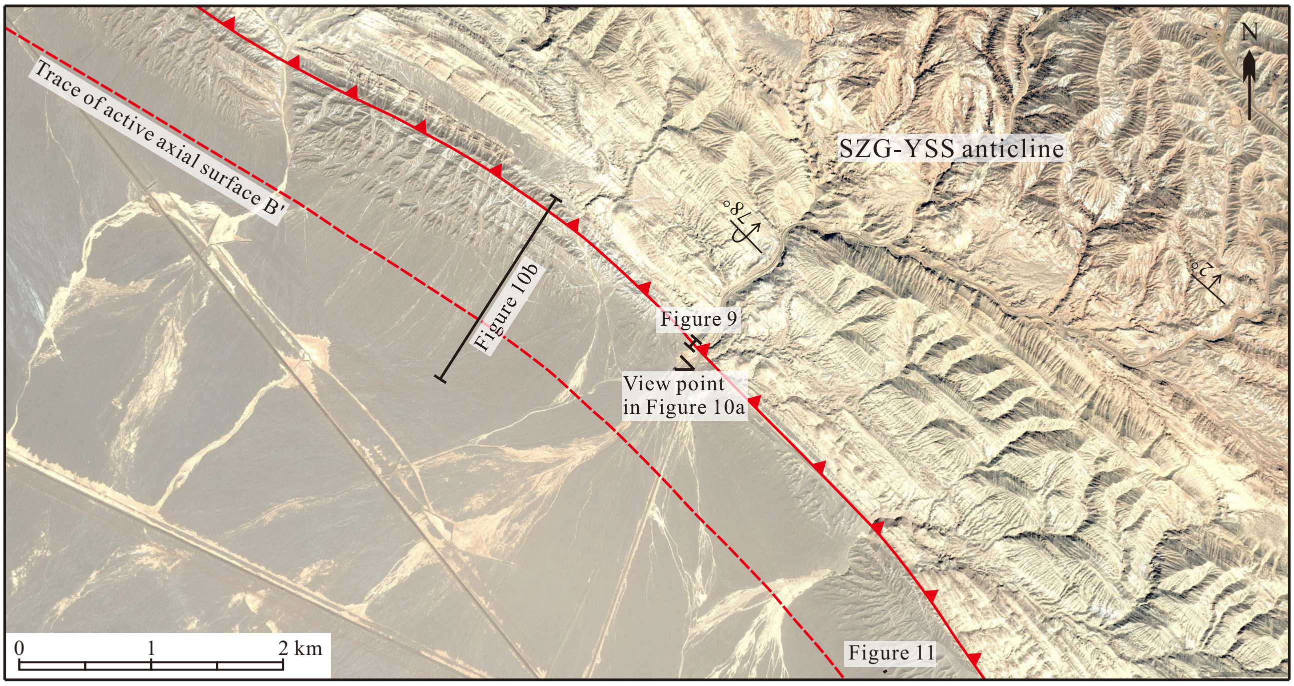

Figure 8. Folded topographic surface and fault scarp along the southwestern edge of northwestern YXL. The red solid line with bars toward the upper plate marks the SZG ramp trace; the red dashed line marks the trace of the active axial surface B'.

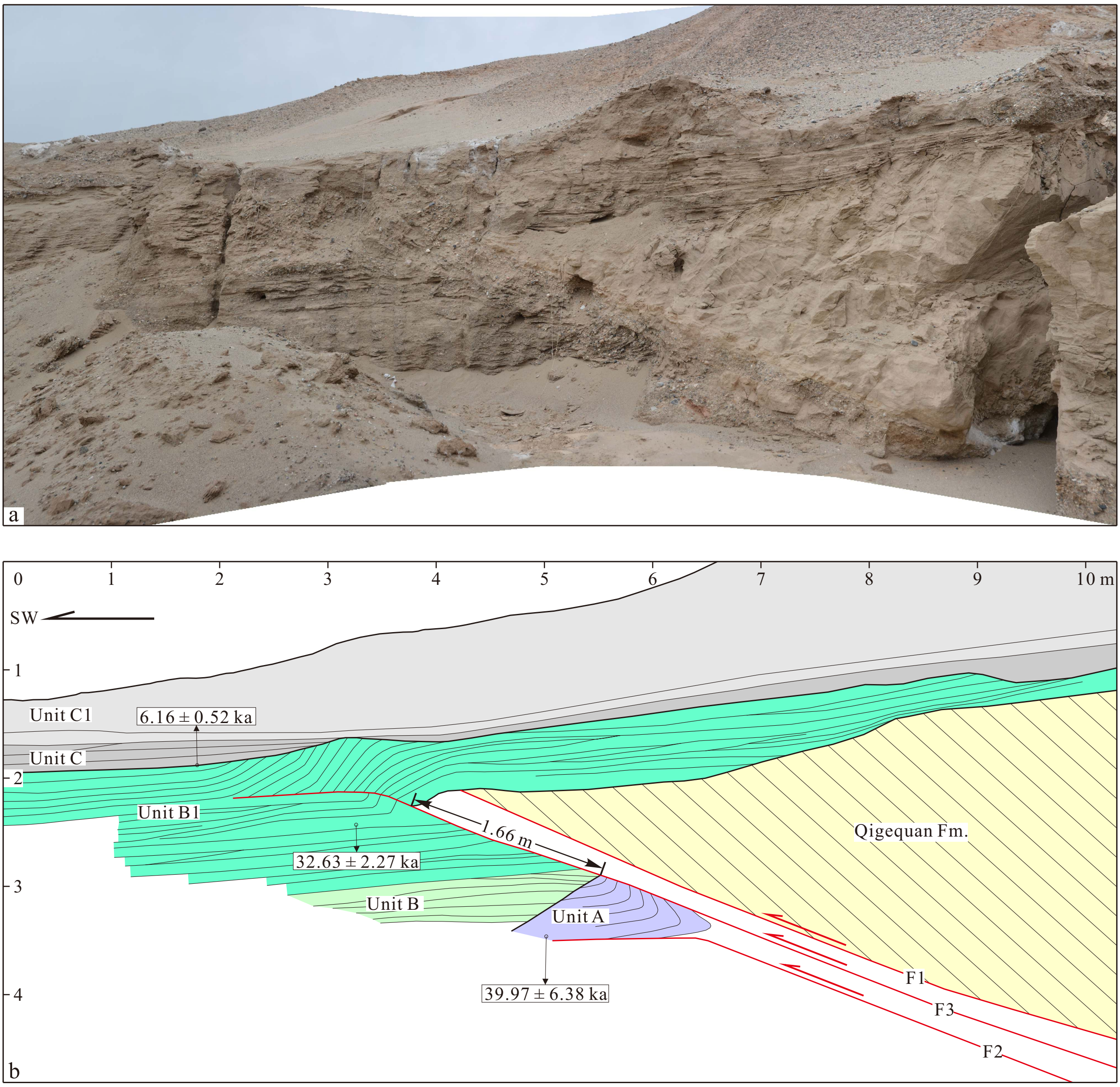

Figure 9. A outcrop photo of deformed alluviums by the SZG ramp (a) and its interpretation (b). Folding of Unit A and Unit B1 represents two thrusting events rupturing the ground surface. The event A happens between 39.77 ± 6.38 ka and 32.63 ± 2.27 ka, and event B1 at 6.16 ± 0.52 ka. Dating results are from Xu et al. (2018a).

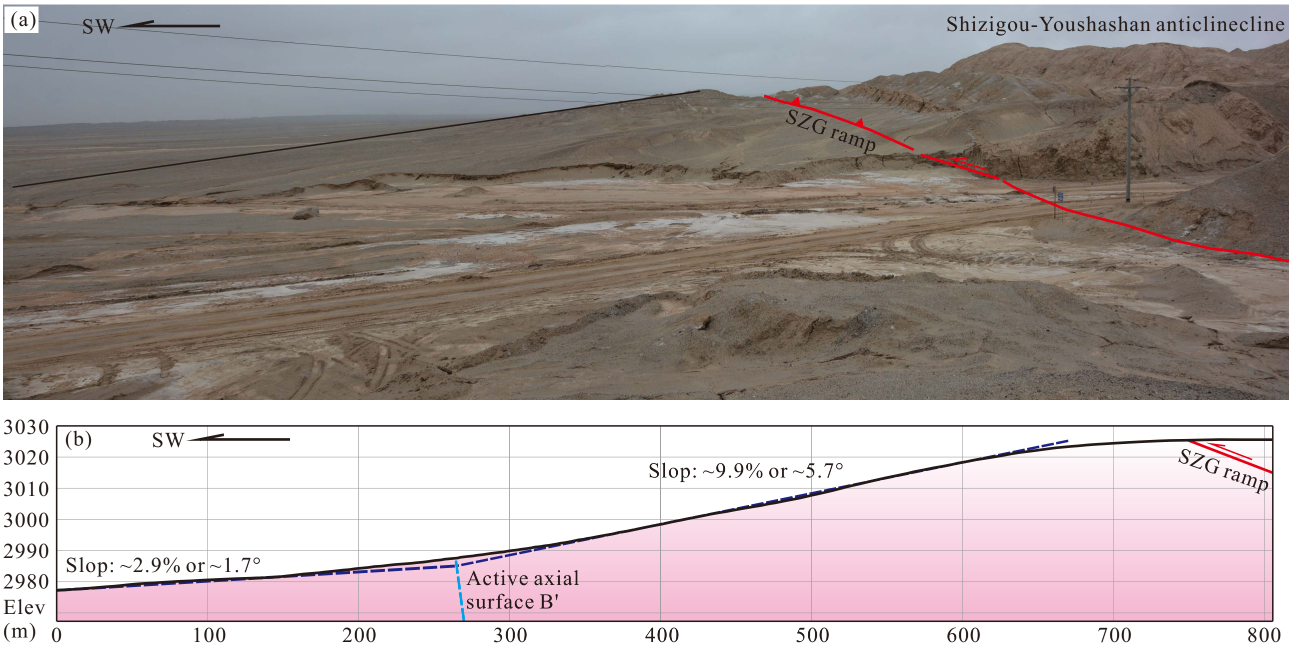

Figure 10. The folded topographic surface and the fault scarp along the southwestern edge of northwestern YXL. (a) A photo of fold scarp and fault scarp. (b) Topographic profile crossing the southwestern edge of YXL. The right side of the photo is the northwestern SZG-YSS anticline. The two topographic inflection points correspond to the outcrop of the SZG ramp and the axial surface of B', respectively.

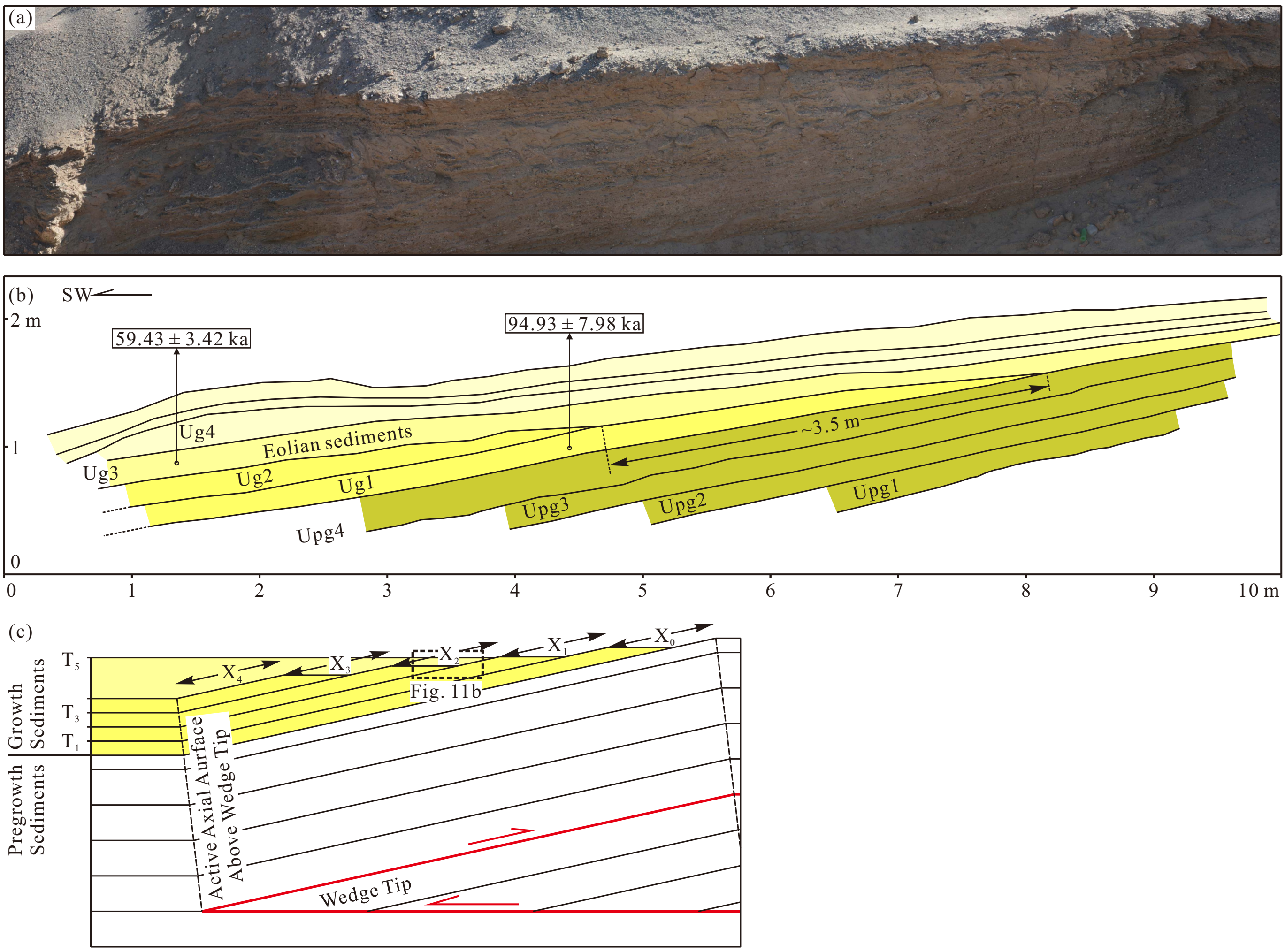

Figure 11. (a) Trench photo of folded alluvium produced by southwest-directed thrusting by the lower SZG wedge structure. (b) Reinterpretation of the trench. Folded Ug1 and Ug2 represents two thrusting events. (c) Simplified model of a terraced hillslope formed on the front limb of a buried wedge thrust structure (modified from Muller and Suppe, 1997). Folding events occur at times Tn, defined by onlapped sediment packages. Terraces were developed above the sediments deposited above strata which had already been folded through an active axial surface. Limb widening by each event is denoted by Xn, which is measured parallel to bedding between outer terrace edges.

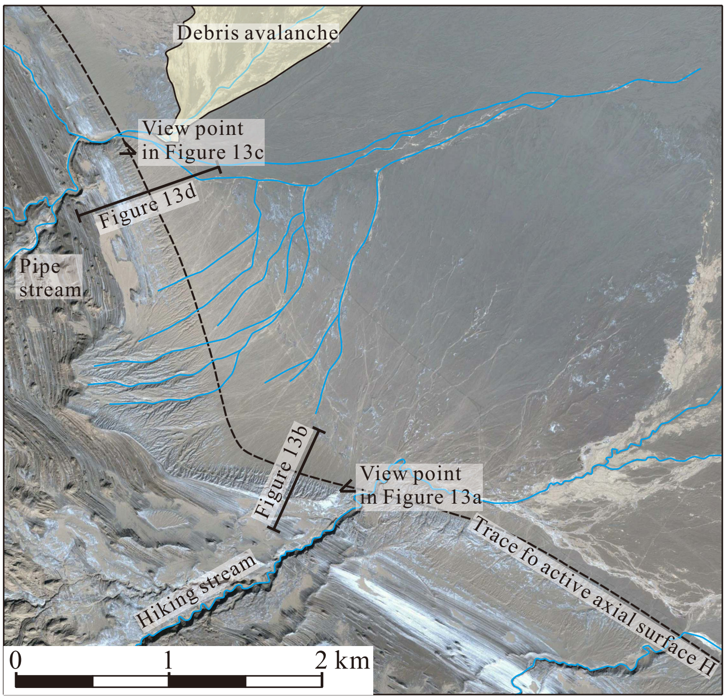

Figure 12. The fold scarp along the northeastern edge of YXL. The Qigequan Formation southwest of the scarp is leveled and patchily covered by evaporates and active sand dunes; the playa northeast of the scarp is somewhere covered by alluviums and debris avalanches. The dashed line marks the trace of trace of the active axial surface H. Figures 13 a, b, c and d are marked.

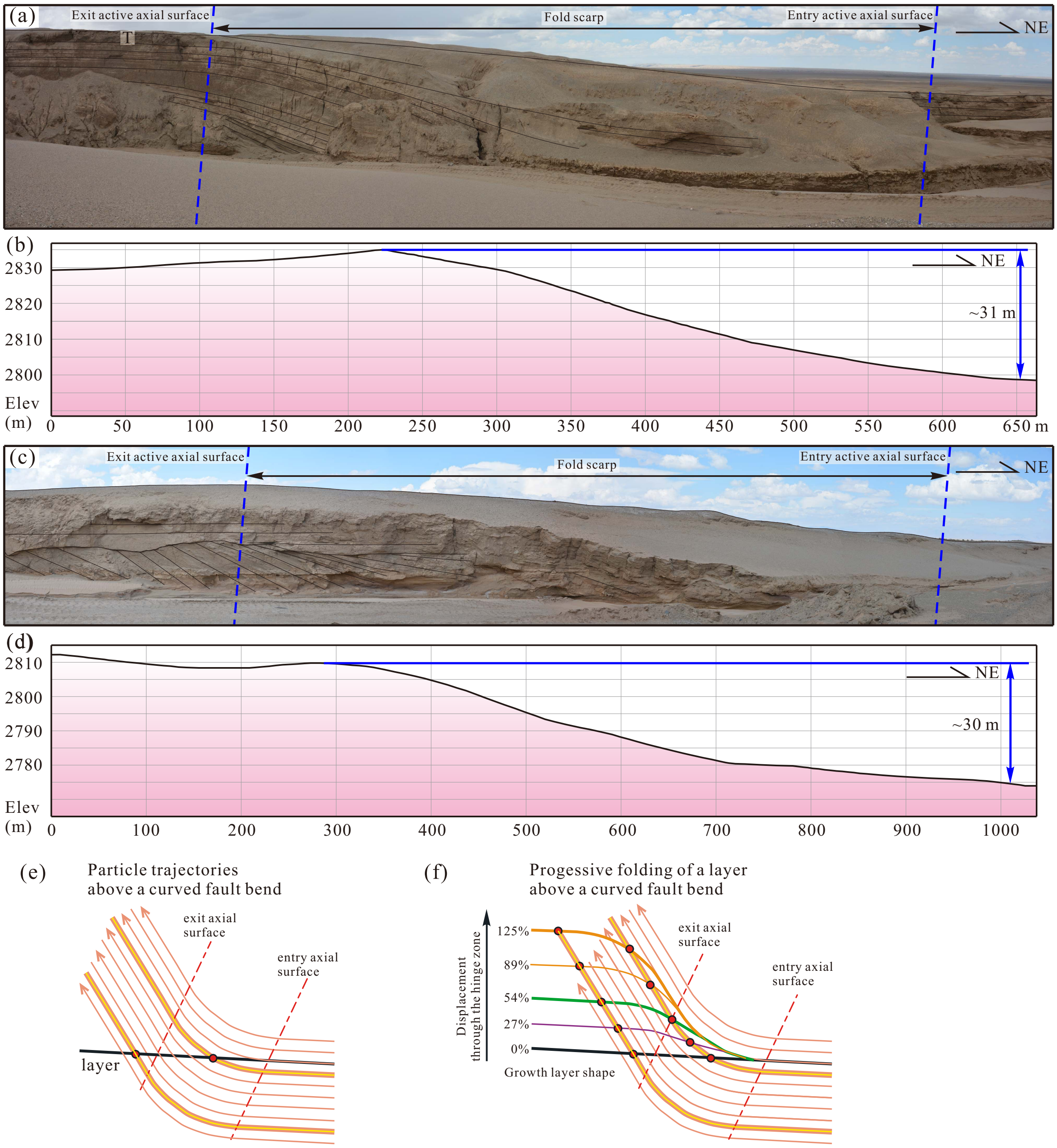

Figure 13. Photos and growth models of the scarp along the northeastern edge of YXL. See Figure 12 for locations of topographic profiles and viewpoints of photos. (a) A horizontally-flipped photo of the scarp at the mouth of the hiking stream. (b) A topographic profile crossing the scarp close to the hiking stream. This profile shows that the scarp height at this site is ~31 meters. (c) A photo of the scarp along the pipe stream. The left end of the photo shows that the recent alluviums cover the northeast-dipping limb of the XSQ-YQZ anticline to form a classic growth unconformity. The angles of the folded alluviums get lower northeastward and contact with the sediments below them in unconformity, disconformity and conformity. (d) A topographic profile crossing the scarp near the pipe stream. This profile shows that the scarp is ~30 m high at this site. (e) A dimensionless wide hinge zone model for changing horizon shape with increasing fractional displacement through a hinge zone with a total change in dip of 56° (from Hubert-Ferrari et al., 2007). (f) Dimensionless templates of fold shapes for incrementally increasing displacement through the hinge. Hinge zone is bounded by entry and exit axial surfaces with an arbitrary width w (from Hubert-Ferrari et al., 2007).